Received: 7 June 2022 | Revised: 25 September 2022 | Accepted: 1 December 2022

DOI: 10.1002/nme.7195

RESEARCH ARTICLE

WILEY

A hybrid strategy blending primal-dual interior point and return mapping methods for a class of hypoelastic-plastic models with memory surface

Yuichi Shintaku[1] | **Fumitoshi Nakamura**[2] | **Kenjiro Terada**[3]

[1]Faculty of Engineering, Information and Systems, University of Tsukuba, Tsukuba, Ibaraki, Japan

[2]Department of Engineering Mechanics and Energy, University of Tsukuba, Tsukuba, Ibaraki, Japan

[3]International Research Institute of Disaster Science, Tohoku University, Aoba-ku, Sendai, Japan

Correspondence
Yuichi Shintaku, Faculty of Engineering, Information and Systems, University of Tsukuba, 1-1-1 Tennoudai, Tsukuba, Ibaraki 305-8573, Japan.
Email: shintaku@kz.tsukuba.ac.jp

Kenjiro Terada, International Research Institute of Disaster Science, Tohoku University, 468-1 Aza-Aoba, Aramaki, Aoba-ku, Sendai 980-8572, Japan.
Email: tei@irides.tohoku.ac.jp

Funding information
Japan Society for the Promotion of Science

Abstract

By blending the primal-dual interior point method (PDIPM) and the return mapping algorithm, we propose a hybrid strategy of implicit stress update for a class of hypoelastic-plastic models with the hardening rule whose evolution is restricted by the memory surface. The inequality constraint relevant to the memory surface is replaced by the equality constraint by the introduction of a slack variable, and the duality gap is gradually reduced by using path-following method. First, we formulate an optimization problem corresponding to the principle of maximum plastic dissipation for the standard von-Mises plasticity with isotropic and kinematic hardening rules and its variant for the model with the memory surface. Next, after function forms employed for the elastic-plastic model are specified, the PDIPM to realize an implicit stress update is briefly reviewed and then applied to the model involving the memory surface to replace the relevant inequality constraint by the equality constraint by the introduction of a slack variable. Then, we present a hybrid scheme that combines the standard return mapping algorithm with the PDIPM. The numerical accuracy of the proposed stress update algorithm for the conventional elastic-plastic model is verified in comparison with the standard return mapping algorithm using iso-error map. Also, targeting a notched round steel bar under cyclic loading with three different amplitudes, we demonstrate the performance for the stress update using the elastic-plastic model with the memory surface. Finally, the capability of the proposed algorithm is proven through a typical real-life example such that a steel bridge is subjected to earthquake for which the residual load carrying capacity must be estimated.

KEYWORDS

Armstrong–Frederick rule, cyclic loading, hardening behavior depending on plastic strain range, kinematic hardening, memory surface, primal-dual interior point method, return mapping algorithm

Abbreviations: A hybrid strategy using primal-dual interior point method for memory surface.

1 | INTRODUCTION

When a steel structure such as a bridge and a nuclear power plant is subjected to earthquake, plastic deformation develops in welds zone and around corners of intersection due to stress concentration and causes fatigue failure; see, for example, Reference 1. To ensure safety of the steel structure, it becomes important to assess plastic deformation under cyclic loading since low-cycle fatigue fracture depends on plastic strain, which is known to follow Coffin–Manson law.[2,3]

In general, to represent the plastic deformation under cyclic loading, an elastic-plastic model with an isotropic hardening rule is combined with a kinematic hardening rule to realize Bauschinger effect. As a result, numerous attempts have been made to develop kinematic hardening rules. Among these developments, Armstrong–Frederick rule[4] is known to successfully predict a nonlinear evolution process of the back stress by introducing a dynamic recovery term into the Prager's linear kinematic hardening rule.[5] Subsequently, a further improved rule, so-called Chaboche model,[6-8] was proposed by superposing several sets of decomposed back stresses with the aim to describe the transient hardening behavior. Since these kinematic hardening rules overestimate the change of back stress associated with ratcheting, a threshold in one or several dynamic recovery terms or a critical state is introduced; see References 9-11. However, it is well known that the conventional elastic-plastic model combined with these kinematic hardening rules is not able to realize the change of hardening behavior under cyclic loading with various ranges of plastic strain. In fact, the change of yield stress depending on the plastic range, which has been observed in our experimental study,[12] cannot be captured by the conventional models. Thus, it is difficult to predict the plastic deformation in the steel structure under cyclic loading, because the range of plastic strain is different by location around the stress concentration.

To realize the dependence of hardening behavior on the largest plastic strain in past, a memory surface in plastic strain space is originally proposed by Chaboche[6] and incorporated into an isotropic hardening rule. Subsequently, the memory surface is generalized by Ohno[13] to accommodate the nonhardening range appearing after reverse loading. A further development[14] is conducted to describe the vanishment of such history dependence after several cycles. The effect of these memory surfaces has been incorporated into isotropic hardening rules,[6,13-20] and also into the kinematic hardening rule[21,22] or both of them.[23] Owing to the inequality constrained condition that the plastic strain exist on or inside the memory surface, these elastic-plastic models can grasp the difference in hardening behavior caused by the plastic strain range. However, since the plastic strain that defines the memory surface is generally determined as a solution of the maximization problem with the yield condition, the involved inequality constraints are coupled with each other. Thus, it appears to be difficult to solve the corresponding initial-value problem for stress update by standard implicit methods such as a conventional return mapping algorithm. Indeed, the nonlinear solution method such as the Newton method is required to obtain the plastic multiplier in implicit methods, while the updated stress satisfying the yield condition is determined up to the plastic strain that is constrained by the memory surface.

In this regard, we are concerned with nonlinear programming methods, since various algorithms to solve constrained optimization problems without dealing with inequality constraints directly. Notable among those is the primal-dual interior point method (PDIPM) that is often employed to bypass the judgment on the inequality conditions; see a review article.[24] For instance, Krabbenhoft et al.[25] demonstrated that the static equilibrium problem with a conventional elastic-plastic model with von-Mises-type, Drucker-Prager-type and multisurface yield functions was formulated as a global optimization problem relevant to the principal of maximum plastic dissipation and could be solved by the finite element method (FEM) combined with the PDIPM with a comparable efficiency to the standard solution method. Also, the PDIPM was successfully applied for a time-independent crystal plasticity model in small deformation theory in Reference 26, suppressing numerical instability due to the arbitrary property of multiple yield conditions. As for applications other than material model, the PDIPM was employed to successfully solve contact problems[27] and was coupled with the Galerkin projection based on a reduced order model.[28]

Against these backgrounds, by effectively blending the PDIPM and the return mapping algorithm, we propose a hybrid strategy of implicit stress update for a class of hypoelastic-plastic models with the hardening rule whose evolution is restricted by the memory surface. The proposed hybrid implicit stress update algorithm is an extension of that of the previous study.[29] That is, while the previous version was developed based on small strain theory, the version originally proposed in this study accommodates a hyoelastic constitutive law with logarithmic rate within the finite strain framework. In addition, the drawback of the previous version that the flow vector is regarded as a constant within a time interval is overcome by the application of the return mapping algorithm to handle the Chaboche model along with the von Mises yield function, which was originally proposed by Lubarda and Besson[30] for the Armstrong–Frederick rule.

First, the principle of maximum plastic dissipation is posed as an optimization problem with the constraint represented by the yield function and is incorporated with the memory surface. Next, after specific function forms for the hardening rules employed in this study are presented, the PDIPM for a standard elastic-plastic model is briefly reviewed and then applied to the model involving the memory surface by reference to the previous study.[25] Then, we propose a hybrid strategy to combine the standard return mapping scheme for the isotropic and kinematic hardening rules with the PDIPM employed to replace the inequality constraint relevant to the memory surface by the equality constraint by the introduction of a slack variable. It should be noted here that the present formulation of the PDIPM is different from that of the previous study[25] in that the stress update is realized by a local optimization within a time interval, which is independent of the global equilibrium equation. The numerical accuracy of the proposed stress update algorithm for the conventional elastic-plastic model is verified in comparison with the standard return mapping algorithm using iso-error map.[31] Also, to demonstrate the performance for the stress update using the elastic-plastic model with the memory surface, we target a notched round steel bar under cyclic loading with three different amplitudes. Finally, the capability of the proposed algorithm is proven through a typical real-life example such that a steel bridge is subjected to earthquake for which the residual load carrying capacity must be estimated.

2 | VARIATIONAL PROBLEM IN HYPOELASTO-PLASTICITY

2.1 | Hypoelastic constitutive law

In general, the additive decomposition of the rate of deformation tensor is assumed for a hypoelasticity-based model in plasticity as

$$\boldsymbol{d} = \boldsymbol{d}^{\mathrm{e}} + \boldsymbol{d}^{\mathrm{p}}, \tag{1}$$

where $\boldsymbol{d}^{\mathrm{e}}$ and $\boldsymbol{d}^{\mathrm{p}}$ are the elastic and plastic components. Then the rate form of the Hooke's law is given as

$$\mathring{\boldsymbol{\tau}} = \mathbb{C}^{\mathrm{e}} : \boldsymbol{d}^{\mathrm{e}}, \tag{2}$$

where $\boldsymbol{\tau} \equiv J\boldsymbol{\sigma}$ is the Kirchhoff stress, $\mathbb{C}^{\mathrm{e}}$ is the fourth-order elastic modulus tensor. Here, $\boldsymbol{\sigma}$ is the Cauchy stress and J is the determinant of the deformation gradient $\boldsymbol{F}$. Also, $\mathring{\bullet}$ denotes an objective co-rotational rate of $\bullet$ defined as

$$\mathring{\bullet} = \dot{\bullet} - \boldsymbol{\Omega} \bullet + \bullet \boldsymbol{\Omega}, \tag{3}$$

where $\dot{\bullet}$ indicates a time derivative of $\bullet$. In this study, the following logarithmic rate[32] is employed:

$$\boldsymbol{\Omega} = \boldsymbol{w} + \sum_{i \neq j}^{N^{\mathrm{dim}}} \left[\frac{1 + (b_i/b_j)}{1 - (b_i/b_j)} + \frac{2}{\ln(b_i/b_j)} \right] \boldsymbol{b}_i \dot{\boldsymbol{b}} \boldsymbol{b}_j, \tag{4}$$

where $\boldsymbol{w}$ is the skew-symmetric part of the velocity gradient $\boldsymbol{L} = \dot{\boldsymbol{F}}\boldsymbol{F}^{-1}$, b_i is the ith eigenvalue of the left Cauchy–Green tensor $\boldsymbol{b} = \boldsymbol{F}\boldsymbol{F}^{\mathrm{T}}$, $\boldsymbol{b}_i$ is the ith eigenprojection of $\boldsymbol{b}$ and N^{dim} is the spatial dimension.

2.2 | Variational problem for elastoplasticity with isotropic and kinematic hardening

Given the yield function $\Phi^{\mathrm{p}}(\boldsymbol{\tau}, \boldsymbol{A})$ defining the admissible space of the Kirchhoff stress $\boldsymbol{\tau} = J\boldsymbol{\sigma}$ as $\Phi^{\mathrm{p}}(\boldsymbol{\tau}, \boldsymbol{A}) \leq 0$, the maximum dissipation principle in plasticity is formulated as the following optimization problems with an inequality constraint:

$$\underset{\{\boldsymbol{\tau},\, \boldsymbol{A}\}}{\text{maximize}} \qquad \boldsymbol{\tau} : \boldsymbol{d}^{\mathrm{p}} - \boldsymbol{A} * \dot{\boldsymbol{\alpha}}. \tag{5}$$

$$\text{subject to} \qquad \Phi^{\mathrm{p}}(\boldsymbol{\tau}, \boldsymbol{A}) \leq 0. \tag{6}$$

Here, $*$ indicates an appropriate inner product defined according to the rank of tensor variables, $\boldsymbol{A}$ and $\dot{\boldsymbol{\alpha}}$. To solve this maximization problem, we define the following Lagrangian function using the multiplier $\dot{\gamma}^{\mathrm{p}} \geq 0$ as

$$\mathcal{L}_0\left(\boldsymbol{\tau}, \boldsymbol{A}, \dot{\gamma}^{\mathrm{p}}\right) = \boldsymbol{\tau} : d^{\mathrm{p}} - \boldsymbol{A} * \dot{\boldsymbol{\alpha}} - \dot{\gamma}^{\mathrm{p}} \Phi^{\mathrm{p}}(\boldsymbol{\tau}, \boldsymbol{A}). \tag{7}$$

Then, the necessary condition for optimality or, equivalently the KKT (Karush–Kuhn–Tucker) condition, is obtained as the following set of equations and inequalities:

$$\begin{cases} \dfrac{\partial \mathcal{L}_0}{\partial \boldsymbol{\tau}} = \boldsymbol{d}^{\mathrm{p}} - \dot{\gamma}^{\mathrm{p}} \dfrac{\partial \Phi^{\mathrm{p}}}{\partial \boldsymbol{\tau}} = \boldsymbol{0}, & (8) \\ \dfrac{\partial \mathcal{L}_0}{\partial \boldsymbol{A}} = -\dot{\boldsymbol{\alpha}} - \dot{\gamma}^{\mathrm{p}} \dfrac{\partial \Phi^{\mathrm{p}}}{\partial \boldsymbol{A}} = \boldsymbol{0}, & (9) \\ \Phi^{\mathrm{p}} \leq 0, \quad \dot{\gamma}^{\mathrm{p}} \geq 0, \quad \Phi^{\mathrm{p}} \dot{\gamma}^{\mathrm{p}} = 0, & (10) \end{cases}$$

where Equations (8), (9), and (10) are the associated flow rule, associated hardening law, and complimentary condition, respectively.

For example, let us employ the following von-Mises' yield function:

$$\Phi^{\mathrm{p}} = \sqrt{\frac{3}{2}} ||\boldsymbol{\eta}|| - \sigma_{\mathrm{y}}(\alpha^{\mathrm{i}}), \tag{11}$$

where σ_{y} is the yield stress postulated by a hardening rule with the scalar-valued hardening variable α^{i}. Also, $||\boldsymbol{\eta}||$ is the norm of the relative stress defined as

$$\boldsymbol{\eta} = \boldsymbol{\tau}_{\mathrm{d}} - \boldsymbol{\beta}, \tag{12}$$

where $\boldsymbol{\tau}_{\mathrm{d}} \equiv \boldsymbol{\tau} - (1/3)\mathrm{tr}(\boldsymbol{\tau})\mathbf{1}$ with $\mathbf{1}$ being the second-order identity tensor and $\boldsymbol{\beta}$ is the back stress. Identifying the current yield stress $\sigma_{\mathrm{y}} = \sigma_{\mathrm{y0}} + \kappa$ with its initial value σ_{y0} and the scalar-valued hardening variable as $\beta \equiv \kappa$ and associating the back stress with the tensor-valued hardening variable $\boldsymbol{\alpha}^{\mathrm{k}}$, we have the set of hardening variables and the corresponding set of thermodynamic forces as $\boldsymbol{\alpha} = \left\{\alpha^{\mathrm{i}}, \boldsymbol{\alpha}^{\mathrm{k}}\right\}$ and $\boldsymbol{A} = \{\beta, \boldsymbol{\beta}\}$, respectively. Thus, the maximization problem in Equation (5) yields

$$\underset{\{\boldsymbol{\tau},\, \beta,\, \boldsymbol{\beta}\}}{\text{maximize}} \qquad \boldsymbol{\tau} : \boldsymbol{d}^{\mathrm{p}} - \beta \dot{\alpha}^{\mathrm{i}} - \boldsymbol{\beta} : \dot{\boldsymbol{\alpha}}^{\mathrm{k}}. \tag{13}$$

$$\text{subject to} \qquad \Phi^{\mathrm{p}}(\boldsymbol{\tau}, \beta, \boldsymbol{\beta}) \leq 0. \tag{14}$$

The corresponding KKT condition becomes

$$\begin{cases} \dfrac{\partial \mathcal{L}_0}{\partial \boldsymbol{\tau}} = \boldsymbol{d}^{\mathrm{p}} - \dot{\gamma}^{\mathrm{p}} \dfrac{\partial \Phi^{\mathrm{p}}}{\partial \boldsymbol{\tau}} = \boldsymbol{0} & \Rightarrow \quad \boldsymbol{d}^{\mathrm{p}} = \dot{\gamma}^{\mathrm{p}} \boldsymbol{N}^{\mathrm{p}}, & (15) \\ \dfrac{\partial \mathcal{L}_0}{\partial \beta} = -\dot{\alpha}^{\mathrm{i}} - \dot{\gamma}^{\mathrm{p}} \dfrac{\partial \Phi^{\mathrm{p}}}{\partial \beta} = 0 & \Rightarrow \quad \dot{\alpha}^{\mathrm{i}} = \dot{\gamma}^{\mathrm{p}}, & (16) \\ \dfrac{\partial \mathcal{L}_0}{\partial \boldsymbol{\beta}} = -\dot{\boldsymbol{\alpha}}^{\mathrm{k}} - \dot{\gamma}^{\mathrm{p}} \dfrac{\partial \Phi^{\mathrm{p}}}{\partial \boldsymbol{\beta}} = \boldsymbol{0} & \Rightarrow \quad \dot{\boldsymbol{\alpha}}^{\mathrm{k}} = \dot{\gamma}^{\mathrm{p}} \boldsymbol{N}^{\mathrm{p}}, & (17) \\ \Phi^{\mathrm{p}} \leq 0, \quad \dot{\gamma}^{\mathrm{p}} \geq 0, \quad \Phi^{\mathrm{p}} \dot{\gamma}^{\mathrm{p}} = 0, & & (18) \end{cases}$$

where we have defined the normal "vector" on the yield surface as

$$\boldsymbol{N}^{\mathrm{p}} \equiv \frac{\partial \Phi^{\mathrm{p}}}{\partial \boldsymbol{\tau}} = \sqrt{\frac{3}{2}} \frac{\boldsymbol{\eta}}{||\boldsymbol{\eta}||} = \sqrt{\frac{3}{2}} \overline{\boldsymbol{N}}^{\mathrm{p}} \quad \text{and} \quad \overline{\boldsymbol{N}}^{\mathrm{p}} \equiv \frac{\boldsymbol{\eta}}{||\boldsymbol{\eta}||}. \tag{19}$$

2.3 | Incorporation with memory surface

To represent the dependency of the hardening behavior on the the plastic strain amplitude, Chaboche[6] incorporated a memory surface defined in the plastic strain space into the an isotropic hardening law. Subsequently, the generalization

was made by Ohno,[13] and followed by Yoshida and Uemori[33] who expressed the surface in the stress space as

$$\Phi^{\mathrm{m}}_{\sigma}(p, \boldsymbol{p}; \boldsymbol{\beta}^{\mathrm{m}}) = ||\boldsymbol{\beta}^{\mathrm{m}} - \boldsymbol{p}|| - p \leq 0, \tag{20}$$

where $\boldsymbol{p}$ and p are the thermodynamic forces representing the origin and radius of the memory surface, respectively. Also, $\boldsymbol{\beta}^{\mathrm{m}}$ is the thermodynamic force conjugate to the plastic strain and may be assumed to be the same as the back stress so that $\boldsymbol{\beta}^{\mathrm{m}} \equiv \boldsymbol{\beta}$ as in Yoshida and Uemori.[33]

Employing the inequality (20) as an additional constraint condition to the maximization problem (13), we have another optimization problem as

$$\begin{aligned} &\text{maximize} && \boldsymbol{\tau} : \boldsymbol{d}^{\mathrm{p}} - \beta\dot{\alpha}^{\mathrm{i}} - \boldsymbol{\beta} : \dot{\boldsymbol{\alpha}}^{\mathrm{k}} - p\dot{q} - \boldsymbol{p} : \dot{\boldsymbol{q}}, && (21)\\ &\text{subject to} && \Phi^{\mathrm{p}}(\boldsymbol{\tau}, \beta, \boldsymbol{\beta}) \leq 0, && (22)\\ & && \Phi^{\mathrm{m}}_{\sigma}(p, \boldsymbol{p}; \boldsymbol{\beta}^{\mathrm{m}}) \leq 0, && (23) \end{aligned}$$

where q and $\boldsymbol{q}$ are internal variables conjugate to p and $\boldsymbol{p}$, respectively. Then, defining the Lagrangian functional as

$$\mathcal{L}_1(\boldsymbol{\tau}, \beta, \boldsymbol{\beta}, p, \boldsymbol{p}) = \boldsymbol{\tau} : \boldsymbol{d}^{\mathrm{p}} - \beta\dot{\alpha}^{\mathrm{i}} - \boldsymbol{\beta} : \dot{\boldsymbol{\alpha}}^{\mathrm{k}} - p\dot{q} - \boldsymbol{p} : \dot{\boldsymbol{q}} - \dot{\gamma}^{\mathrm{p}}\Phi^{\mathrm{p}}(\boldsymbol{\tau}, \beta, \boldsymbol{\beta}) - \dot{\gamma}^{\mathrm{m}}\Phi^{\mathrm{m}}_{\sigma}(p, \boldsymbol{p}; \boldsymbol{\beta}^{\mathrm{m}}), \tag{24}$$

we have the following KKT condition:

$$\begin{cases} \dfrac{\partial \mathcal{L}_1}{\partial \boldsymbol{\tau}} = \boldsymbol{d}^{\mathrm{p}} - \dot{\gamma}^{\mathrm{p}}\dfrac{\partial \Phi^{\mathrm{p}}}{\partial \boldsymbol{\tau}} = \boldsymbol{0} & \Rightarrow \quad \boldsymbol{d}^{\mathrm{p}} = \dot{\gamma}^{\mathrm{p}}\boldsymbol{N}^{\mathrm{p}}, & (25)\\ \dfrac{\partial \mathcal{L}_1}{\partial \beta} = -\dot{\alpha}^{\mathrm{i}} - \dot{\gamma}^{\mathrm{p}}\dfrac{\partial \Phi^{\mathrm{p}}}{\partial \beta} = 0 & \Rightarrow \quad \dot{\alpha}^{\mathrm{i}} = \dot{\gamma}^{\mathrm{p}}, & (26)\\ \dfrac{\partial \mathcal{L}_1}{\partial \boldsymbol{\beta}} = -\dot{\boldsymbol{\alpha}}^{\mathrm{k}} - \dot{\gamma}^{\mathrm{p}}\dfrac{\partial \Phi^{\mathrm{p}}}{\partial \boldsymbol{\beta}} = \boldsymbol{0} & \Rightarrow \quad \dot{\boldsymbol{\alpha}}^{\mathrm{k}} = \dot{\gamma}^{\mathrm{p}}\boldsymbol{N}^{\mathrm{p}}, & (27)\\ \dfrac{\partial \mathcal{L}_1}{\partial p} = -\dot{q} - \dot{\gamma}^{\mathrm{m}}\dfrac{\partial \Phi^{\mathrm{m}}_{\text{œ}}}{\partial p} = 0 & \Rightarrow \quad \dot{q} = \dot{\gamma}^{\mathrm{m}}, & (28)\\ \dfrac{\partial \mathcal{L}_1}{\partial \boldsymbol{p}} = -\dot{\boldsymbol{q}} - \dot{\gamma}^{\mathrm{m}}\dfrac{\partial \Phi^{\mathrm{m}}_{\text{œ}}}{\partial \boldsymbol{p}} = \boldsymbol{0} & \Rightarrow \quad \dot{\boldsymbol{q}} = \dot{\gamma}^{\mathrm{m}}\boldsymbol{N}^{\mathrm{m}}_{\text{œ}}, & (29)\\ \Phi^{\mathrm{p}} \leq 0, \quad \dot{\gamma}^{\mathrm{p}} \geq 0, \quad \Phi^{\mathrm{p}}\dot{\gamma}^{\mathrm{p}} = 0 & & (30)\\ \Phi^{\mathrm{m}}_{\text{œ}} \leq 0, \quad \dot{\gamma}^{\mathrm{m}} \geq 0, \quad \Phi^{\mathrm{m}}_{\text{œ}}\dot{\gamma}^{\mathrm{m}} = 0 & & (31) \end{cases}$$

where the normal "vector" on the memory surface have been defined as

$$\boldsymbol{N}^{\mathrm{m}}_{\sigma} \equiv \frac{\partial \Phi^{\mathrm{m}}_{\sigma}}{\partial \boldsymbol{p}}. \tag{32}$$

Meanwhile, the memory surface originally defined by Chaboche[6] and subsequently generalized by Ohno[13] is given in the plastic strain space as

$$\Phi^{\mathrm{m}}_{\varepsilon}(q, \boldsymbol{q}; \boldsymbol{\varepsilon}^{\mathrm{p}}) = ||\boldsymbol{\varepsilon}^{\mathrm{p}} - \boldsymbol{q}|| - q \leq 0, \tag{33}$$

where the plastic strain $\boldsymbol{\varepsilon}^{\mathrm{p}}$ is defined by the following time integral:

$$\boldsymbol{\varepsilon}^{\mathrm{p}} = \int_T \boldsymbol{d}^{\mathrm{p}} \mathrm{d}T. \tag{34}$$

Also, the normal "vector" on it is defined as

$$\boldsymbol{N}^{\mathrm{m}}_{\varepsilon} \equiv \frac{\partial \Phi^{\mathrm{m}}_{\varepsilon}}{\partial \boldsymbol{q}}. \tag{35}$$

If $\boldsymbol{\beta}^{\mathrm{m}}$ is identified with $\boldsymbol{\beta}$ and if the Prager's linear hardening rule $\dot{\boldsymbol{\beta}}^{\mathrm{m}} = L^{\mathrm{m}}\boldsymbol{d}^{\mathrm{p}}$ is assumed with $\boldsymbol{d}^{\mathrm{p}}$ being identified with $\dot{\boldsymbol{\alpha}}^{\mathrm{k}}$, the expressions in Equations (20) and (33) are found to be identical.[33] Here, L^{m} is a material constant. Although the

employment of other hardening rules may not assure the consistency, most of the relationships above are expected to be acceptable. It should be noted that, regarding $\boldsymbol{\beta}^{\mathrm{m}}$ in (20) as a function of the plastic strain (34), we have transformed the memory surface (20) in the stress space into the one in the strain space as in Equation (33).

2.4 | Specific forms of hardening rules

To represent the isotropic hardening behavior evolving subject to the constraint of the memory surface, we define the following yield stress

$$\sigma_y = \sigma_{\mathrm{y0}} + \kappa_{\mathrm{y}}(\alpha^{\mathrm{i}}) + \kappa_{\mathrm{m}}(\alpha^{\mathrm{m}}), \tag{36}$$

where $\sigma_{\mathrm{y0}} + \kappa_{\mathrm{y}}(\alpha_{\mathrm{y}})$ is a conventional hardening function with σ_{y0} being the initial yield stress. In this study, we employ is the conventional Voce's hardening rule given as

$$\kappa_{\mathrm{y}}(\alpha^{\mathrm{i}}) = L_{\mathrm{y}}\alpha^{\mathrm{i}} + R_{\mathrm{y}}(1 - \exp(-r_{\mathrm{y}}\alpha^{\mathrm{i}})). \tag{37}$$

where L_{y}, R_{y}, and r_{y} are material constants. Here, using Equation (26), we have

$$\alpha^{\mathrm{i}} = \int_T \dot{\gamma}^{\mathrm{p}} \mathrm{d}T, \tag{38}$$

which is regarded as the accumulated plastic strain. Also, κ_{m} is an additional isotropic hardening function depending on the evolution of the memory surface. Similarly to the model we proposed Reference 20, we assume the following function form for κ_{m}:

$$\kappa_{\mathrm{m}}(\alpha^{\mathrm{m}}) = L^{\mathrm{q}}(q)\alpha^{\mathrm{m}}, \tag{39}$$

where $L^{\mathrm{q}}(q)$ is a function of the radius of the memory surface q, and α_{m} is the internal variable whose evolution law is defined as follows:

$$\dot{\alpha}^{\mathrm{m}} = \dot{\alpha}^{\mathrm{i}} - \dot{q}. \tag{40}$$

Thus, α^{m} is an increasing function of α^{i}. In addition, the hardening modulus $L^{\mathrm{q}}(q)$ is assumed to evolve according to the following rule:

$$\dot{L}^{\mathrm{q}} = \left(m_1 q^2 + m_2 q + m_3\right)\dot{q}, \tag{41}$$

where m_1, m_2, and m_3 are nonnegative material constants.

The evolution law for q was suggested by Ohno[13] as

$$\dot{q} = \left(\boldsymbol{d}^{\mathrm{p}} : \overline{\boldsymbol{N}}^{\mathrm{m}}_{\varepsilon}\right)\mathrm{H}(\Phi^{\mathrm{m}}_{\varepsilon}) = \dot{\gamma}^{\mathrm{p}}\left(\overline{\boldsymbol{N}}^{\mathrm{p}} : \overline{\boldsymbol{N}}^{\mathrm{m}}_{\varepsilon}\right)\mathrm{H}(\Phi^{\mathrm{m}}_{\varepsilon}), \tag{42}$$

where $\mathrm{H}(\bullet)$ is the Heaviside function such that if $\bullet < 0$, then $\mathrm{H}(\bullet) = 0$ and if $\bullet \geq 0$, then $\mathrm{H}(\bullet) = 1$. Thus, $\dot{q} = \dot{\gamma}^{\mathrm{m}} \geq 0$ is guaranteed. Also, according to Equation (33), if a plastic strain is on the memory surface, that is, $\Phi^{\mathrm{m}}_{\varepsilon} = 0$, we have $\dot{q} \geq 0$, while $\dot{q} = 0$ holds if $\Phi^{\mathrm{m}}_{\varepsilon} < 0$. On the other hand, the evolution law[13] for $\boldsymbol{q}$ that is the origin of the memory surface is assumed to be expressed by the following form:

$$\dot{\boldsymbol{q}} = \dot{q}\overline{\boldsymbol{N}}^{\mathrm{m}}_{\varepsilon} = \dot{\gamma}^{\mathrm{p}}(\overline{\boldsymbol{N}}^{\mathrm{p}} : \overline{\boldsymbol{N}}^{\mathrm{m}}_{\varepsilon})\mathrm{H}(\Phi^{\mathrm{m}}_{\varepsilon})\overline{\boldsymbol{N}}^{\mathrm{m}}_{\varepsilon}. \tag{43}$$

Ohno[13] suggested to multiply c and $1 - c$ by (42) and (43), respectively, to adjust the contribution of each effect. However, the same simplification as Zhu et al.[22] is employed, that is, $c = 1$ so that $\boldsymbol{q} = \boldsymbol{0}$, since the nonhardening range was not observed from our experimental results.[12]

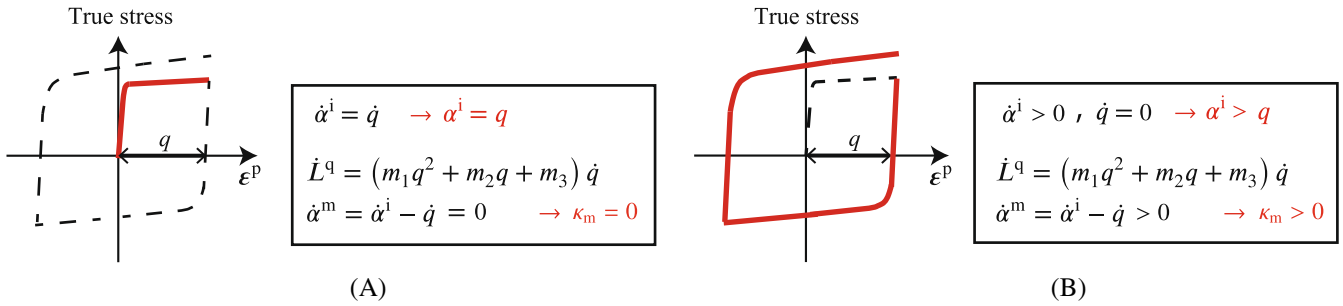

FIGURE 1 Isotropic hardening behavior depending on memory surface. (A) monotonic loading; (B) cyclic loading after monotonic loading

It is confirmed from Equation (28) ($\dot{q} = \dot{\gamma}^{\mathrm{m}}$) that the relationships postulated for q are consistent with the complimentary condition in Equation (31). That is, under monotonic loading as shown in Figure 1A, the radius q and α^{i} coincide. Then, only L^{q} evolves according to Equation (41) because $\dot{q} > 0$, while α^{m} does not because $\dot{q} = \dot{\alpha}^{\mathrm{i}}$ in Equation (40). In other words, since $\dot{\alpha}_{\mathrm{m}} = 0$, the contribution of the memory surface to the isotropic hardening is zero, that is, $\kappa_{\mathrm{m}}(\alpha^{\mathrm{m}}) = 0$. On the other hand, under cyclic loading as shown in Figure 1B, since $\dot{q} = 0$ because $\Phi^{\mathrm{m}}_{\varepsilon} = 0$, the accumulated plastic strain α^{i} becomes larger than the radius of the memory surface q. Then, whereas L^{q} in Equation (41) does not evolve, only α_{m} evolves according to Equation (40). In summary, the isotropic hardening is driven by $\kappa_{\mathrm{m}}(\alpha_{\mathrm{m}}) > 0$ under cyclic loading, while the hardening modulus $L^{\mathrm{q}}(q)$ increases on its own under monotonic loading.

To represent the kinematic hardening behavior, the objective rate of the back stress is expressed as the sum of stress rates as

$$\mathring{\boldsymbol{\beta}} = \sum_{k=1}^{N^{\mathrm{kin}}} \mathring{\boldsymbol{\beta}}^{(k)}, \tag{44}$$

Adopting the Chaboche model,[6-8] which is known as an extension of Armstrong-Frederick rule,[4] we postulate each stress rate as

$$\mathring{\boldsymbol{\beta}}^{(k)} = a_k \boldsymbol{d}^{\mathrm{p}} - b_k \dot{\gamma}^{\mathrm{p}} \boldsymbol{\beta}^{(k)}, \tag{45}$$

where a_k and b_k are material constants. As mentioned before, the relationship between the hardening rule in Equation (27) and the evolution equation (45) is not consistent.

3 | IMPLICIT STRESS UPDATE FOR ELASTOPLASTICITY WITH MEMORY SURFACE

A hybrid strategy of stress update for an elastoplastic model with memory surface is proposed by blending the conventional return mapping algorithm and the PDIPM. First, the PDIPM for the standard elastic-plastic model is formulated in line with the principal of maximum plastic dissipation by reference to previous study.[25] Second, the PDIPM is extended to incorporate the model with memory surface. Finally, we originally present a hybrid formulation and perform its time-discretization to realize a new implicit algorithm for an elastoplastic constitutive law with memory surface.

3.1 | PDIPM for standard elastoplasticity

Prior to proposing the hybrid implicit stress update algorithm, we present the PDIPM for the standard elastic-plastic model with isotropic and kinematic hardening by referring to Krabbenhoft et al.[25]

In line with a PDIPM originally proposed by Yamashita,[34] the maximization problem (13) is rewritten by the introduction of a logarithmic barrier function $\mu_1 \log s$ with μ_1 being a positive small value as follows:

$$\underset{\{\boldsymbol{\tau},\,\beta,\,\boldsymbol{\beta}\}}{\text{maximize}} \quad \boldsymbol{\tau} : \boldsymbol{d}^{\mathrm{p}} - \beta\dot{\alpha}^{\mathrm{i}} - \boldsymbol{\beta} : \dot{\boldsymbol{\alpha}}^{\mathrm{k}} + \mu_1 \log s, \tag{46}$$

$$\text{subject to} \quad \Phi^{\mathrm{p}}(\boldsymbol{\tau}, \beta, \boldsymbol{\beta}) + s = 0, \tag{47}$$

where the inequality constrain (14) is transformed to the equality constraint by the introduction of slack variable $s > 0$. Then, the Lagrangian functional is defined as

$$\mathcal{L}_0^{\mathrm{PD}}(\boldsymbol{\tau}, \beta, \boldsymbol{\beta}, s) = \boldsymbol{\tau} : \boldsymbol{d}^{\mathrm{p}} - \beta\dot{\alpha}^{\mathrm{i}} - \boldsymbol{\beta} : \dot{\boldsymbol{\alpha}}^{\mathrm{k}} + \mu_1 \log s - \dot{\gamma}^{\mathrm{p}} \left(\Phi^{\mathrm{p}}(\boldsymbol{\tau}, \beta, \boldsymbol{\beta}) + s \right), \tag{48}$$

where $\dot{\gamma}^{\mathrm{p}}$ is the Lagrange multiplier. The stationary point of this Lagrangian function can be obtained as

$$\begin{cases} \dfrac{\partial \mathcal{L}_0^{\mathrm{PD}}}{\partial \boldsymbol{\tau}} = \boldsymbol{d}^{\mathrm{p}} - \dot{\gamma}^{\mathrm{p}} \dfrac{\partial \Phi^{\mathrm{p}}}{\partial \boldsymbol{\tau}} = \boldsymbol{0} & \Rightarrow \quad \boldsymbol{d}^{\mathrm{p}} = \dot{\gamma}^{\mathrm{p}} \boldsymbol{N}^{\mathrm{p}}. & (49) \\ \dfrac{\partial \mathcal{L}_0^{\mathrm{PD}}}{\partial \beta} = -\dot{\alpha}^{\mathrm{i}} - \dot{\gamma}^{\mathrm{p}} \dfrac{\partial \Phi^{\mathrm{p}}}{\partial \beta} = 0 & \Rightarrow \quad \dot{\alpha}^{\mathrm{i}} = \dot{\gamma}^{\mathrm{p}}. & (50) \\ \dfrac{\partial \mathcal{L}_0^{\mathrm{PD}}}{\partial \boldsymbol{\beta}} = -\dot{\boldsymbol{\alpha}}^{\mathrm{k}} - \dot{\gamma}^{\mathrm{p}} \dfrac{\partial \Phi^{\mathrm{p}}}{\partial \boldsymbol{\beta}} = \boldsymbol{0} & \Rightarrow \quad \dot{\boldsymbol{\alpha}}^{\mathrm{k}} = \dot{\gamma}^{\mathrm{p}} \boldsymbol{N}^{\mathrm{p}}. & (51) \\ \dfrac{\partial \mathcal{L}_0^{\mathrm{PD}}}{\partial \dot{\gamma}^{\mathrm{p}}} = -\Phi^{\mathrm{p}}(\boldsymbol{\tau}, \beta, \boldsymbol{\beta}) - s = 0 & \Rightarrow \quad \Phi^{\mathrm{p}}(\boldsymbol{\tau}, \beta, \boldsymbol{\beta}) + s = 0. & (52) \\ \dfrac{\partial \mathcal{L}_0^{\mathrm{PD}}}{\partial s} = \dfrac{\mu_1}{s} - \dot{\gamma}^{\mathrm{p}} = 0 & \Rightarrow \quad \mu_1 - \dot{\gamma}^{\mathrm{p}} s = 0. & (53) \end{cases}$$

This format with the barrier function is the same as that of Krabbenhoft et al.,[25] in which the relevant variational formulation is presented for conventional elastic-plastic models.

As will be presented in Section 2.4, when a standard plasticity model is employed and time discretization is applied to Equations (49), (50), and (51), the reduced set of simultaneous equations for unknowns, $s > 0$ and $\dot{\gamma}^{\mathrm{p}}$, is obtained as follows:

$$\begin{cases} \Phi^{\mathrm{p}} + s = 0. & (54) \\ \mu_1 - \dot{\gamma}^{\mathrm{p}} s = 0. & (55) \end{cases}$$

Here, the former and latter equations correspond to the modified yield function and complementary condition, respectively. When specific function forms of $\beta \equiv \kappa$ and $\boldsymbol{\beta}$ are provided as functions of α^{i} and $\boldsymbol{\alpha}^{\mathrm{k}} \equiv \boldsymbol{\varepsilon}^{\mathrm{p}}$, respectively, the number of equations is reduced from five down to two after time-discretization. Then, the discretized problem consists of a set of nonlinear algebraic equations $s > 0$ and $\Delta\gamma^{\mathrm{p}}$.

To obtained the above saddle point, we employ the path-following method as a common maneuver. That is, Equations (54) and (55) are numerically solved for $\dot{\gamma}^{\mathrm{p}}$ and s by Newton method, while the duality gap μ_1 is gradually brought close to zero. This algorithm enables us to obtain the solution of the optimization problem Equation (46) and (47) that is supposed to be the same as that of the original problem without making a true or false determination of the inequality constraint. In other words, the primal and dual problem can concurrently be solved while the complementary condition (55) is satisfied with a decrease in the duality gap that represents the difference between these two objective functions.

Nevertheless, the numerical algorithm tends to be slightly complex due to an exception processing to have $s \geq 0$. In fact, Krabbenhoft et al.[25] presented a measure to intentionally set s at a small positive value if s becomes negative during an iteration process. To avoid this issue, we replace s in Equation (48) with s_1^2 so that Equations (54) and (55) are modified as follows:

$$\begin{cases} \Phi^{\mathrm{p}} + s_1^2 = 0. & (56) \\ \mu_1 - \dot{\gamma}^{\mathrm{p}} s_1^2 = 0. & (57) \end{cases}$$

It should be noted that the optimization presented here is locally performed, while the previous study[25] incorporates the optimization into a set of global governing equations.

3.2 | PDIPM for elastoplasticity with memory surface

When a standard elastic-plastic model with isotropic and/or kinematic hardening rules is considered, the computational efficiency of the PDIPM is poor in comparison with the conventional return mapping algorithm. In fact, the nonlinear algebraic equation is solved just once in the return mapping algorithm, whereas it is necessary to solve that Equations (56) and (57) repeatedly while gradually bringing the duality gap closer to zero. In other words, at each iterative step for obtaining the global equilibrium, the nonlinear simultaneous equations must be solved for the number of times repeated. Thus, the application of the PDIPM to conventional elastic-plastic models is not efficient at all in terms of computational efficiency. However, when the standard elastic-plastic model is combined with the memory surface as presented in Section 2.3, the stress update process with the standard return mapping algorithm hardly obtain the unique solution in a stable manner. This is because inequality constraint (23) depends on the plastic strain that is determined by the admissible stress satisfying another inequality constraint (22); see Equation (33). In such cases, the application of the PDIPM is effective. In this subsection, the formulation in the previous subsection is extended to accommodate the evolution equations for the additional internal state variables subject to the constraint (23) defining the memory surface.

Applying the same line described in the previous subsection, we transform the optimization problem (21) with inequality constrains (22) and (23) as

$$\begin{aligned} &\text{maximize} && \boldsymbol{\tau} : \boldsymbol{d}^{\mathrm{p}} - \beta\dot{\alpha}^{\mathrm{i}} - \boldsymbol{\beta} : \dot{\boldsymbol{\alpha}}^{\mathrm{k}} - p\dot{q} + \mu_1 \log s_1^2 + \mu_2 \log s_2^2, && (58)\\ &\text{subject to} && \Phi^{\mathrm{p}}(\boldsymbol{\tau}, \beta, \boldsymbol{\beta}) + s_1^2 = 0, && (59)\\ &&& \Phi_{\sigma}^{\mathrm{m}}(p; \boldsymbol{\beta}^{\mathrm{m}}) + s_2^2 = 0, && (60) \end{aligned}$$

in which we have reflected $\boldsymbol{q} \equiv \boldsymbol{0}$ or, equivalently, $\boldsymbol{p} \equiv \boldsymbol{0}$. The Lagrangian functional is given as

$$\mathcal{L}_1^{\mathrm{PD}}(\boldsymbol{\tau}, \beta, \boldsymbol{\beta}, p, s_1, s_2) = \mathcal{L}_0^{\mathrm{PD}}(\boldsymbol{\tau}, \beta, \boldsymbol{\beta}, s_1) - p\dot{q} + \mu_2 \log s_2^2 - \dot{\gamma}^{\mathrm{m}}\left(\Phi_{\sigma}^{\mathrm{m}}(p; \boldsymbol{\beta}^{\mathrm{m}}) + s_2^2\right). \tag{61}$$

The stationary point of this Lagrangian that is equivalent to the set of optimal solutions of the original constrained maximization problem defined above reads to Equations (25)–(28) along with the following set of nonlinear simultaneous equations:

$$\begin{cases} \Phi^{\mathrm{p}} + s_1^2 = 0. & (62)\\ \mu_1 - \dot{\gamma}^{\mathrm{p}} s_1^2 = 0. & (63)\\ \Phi_{\sigma}^{\mathrm{m}} + s_2^2 = 0. & (64)\\ \mu_2 - \dot{q} s_2^2 = 0. & (65) \end{cases}$$

Here, Equations (62) and (63) are the same as Equations (56) and (57), respectively, and Equations (64) and (65) are the constraint condition for the memory surface and the corresponding complementary condition, respectively.

Again, there is no need for a true or false determination of both of the inequality constraints (22) and (23). Thus, the set of solutions of Equations (62)–(65) can stably be obtained, even though the internal state variables associated with the memory surface are determined by the admissible stress satisfying the yield condition. Nevertheless, as mentioned above, the PDIPM must be time-consuming. This motivates us to combine the local return mapping algorithm for the evolution equations associated with the yield condition and the PDIPM for those of the memory surface as will be presented below.

3.3 | Hybrid stress update for elastoplasticity with memory surface

We propose a new implicit stress update scheme for elastoplasticity with memory surface by combining a conventional return mapping algorithm that is employed to satisfy the yield condition and the PDIPM to satisfy the memory surface condition. Because of this feature, the resulting stress update algorithm is hybrid. Having said that, to formulate the corresponding optimization problem, we simply replace the constraint in Equation (59) by the original inequality constraint

in Equation (22) as

$$\begin{aligned} &\text{maximize} && \boldsymbol{\tau} : \boldsymbol{d}^{\mathrm{p}} - \beta\dot{\alpha}^{\mathrm{i}} - \boldsymbol{\beta} : \dot{\boldsymbol{\alpha}}^{\mathrm{k}} - p\dot{q} + \mu_2 \log s_2^2. && (66)\\ &\text{subject to} && \Phi^{\mathrm{p}}(\boldsymbol{\tau}, \beta, \boldsymbol{\beta}) \leq 0. && (67)\\ & && \Phi_{\sigma}^{\mathrm{m}}(p; \boldsymbol{\beta}^{\mathrm{m}}) + s_2^2 = 0. && (68) \end{aligned}$$

To remove the constraint conditions, the Lagrangian functional is introduced in a normal fashion as

$$\mathcal{L}^{\mathrm{Hybrid}}(\boldsymbol{\tau}, \beta, \boldsymbol{\beta}, p) = \boldsymbol{\tau} : \boldsymbol{d}^{\mathrm{p}} - \beta\dot{\alpha}^{\mathrm{i}} - \boldsymbol{\beta} : \dot{\boldsymbol{\alpha}}^{\mathrm{k}} - p\dot{q} - \dot{\gamma}^{\mathrm{p}}\Phi^{\mathrm{p}}(\boldsymbol{\tau}, \beta, \boldsymbol{\beta}) + \mu_2 \log s_2^2 - \dot{\gamma}^{\mathrm{m}}\left(\Phi_{\sigma}^{\mathrm{m}}(p; \boldsymbol{\beta}^{\mathrm{m}}) + s_2^2\right), \tag{69}$$

Then, the following KKT conditions are obtained:

$$\begin{cases} \boldsymbol{d}^{\mathrm{p}} = \dot{\gamma}^{\mathrm{p}}\boldsymbol{N}^{\mathrm{p}}. & (70)\\ \dot{\alpha}^{\mathrm{i}} = \dot{\gamma}^{\mathrm{p}}. & (71)\\ \dot{\boldsymbol{\alpha}}^{\mathrm{k}} = \dot{\gamma}^{\mathrm{p}}\boldsymbol{N}^{\mathrm{p}}. & (72)\\ \Phi^{\mathrm{p}} \leq 0, \quad \dot{\gamma}^{\mathrm{p}} \geq 0, \quad \Phi^{\mathrm{p}}\dot{\gamma}^{\mathrm{p}} = 0. & (73)\\ \dot{q} = \dot{\gamma}^{\mathrm{m}}. & (74)\\ \Phi_{\sigma}^{\mathrm{m}} + s_2^2 = 0. & (75)\\ \mu_2 - \dot{\gamma}^{\mathrm{m}} s_2^2 = 0. & (76) \end{cases}$$

Here, the first four relationships associated with the flow and hardening rules subjected to the yield condition are solved with the return mapping method, while the remaining three are solved with the PDIPM. However, we realize that the both sets of relationships are coupled with each other when adopting the specific function forms provided in Section 2.4. Therefore, an efficient numerical algorithm needs to be developed and will be presented in the next section.

4 | TIME DISCRETIZATION AND NUMERICAL ALGORITHM

The set of governing equations derived in the previous sections is discretized in time, and the corresponding numerical algorithm for implicit stress update is established.

4.1 | Time discretization

The backward Euler scheme is employed for time discretization. Adopting the von-Mises yield function with the Chaboche model, we apply the return mapping method to Equations (70), (71), (72), and (73) by reference to that originally proposed by Lubarda and Benson[30] to handle the Armstrong–Frederick rule. The derived algebraic equations are combined with the discretized forms of Equations (74), (75), and (76) to compose the set of simultaneous nonlinear equations. In the formulation, $\bullet_n$ and $\bullet_{n+1}$ denote the values of $\bullet$ at time T_n and T_{n+1}, respectively, and $\Delta\bullet$ is the increment of $\bullet$ between T_n and T_{n+1}. Also, $\bullet$ in $\diamond[\bullet]$ is the argument of function $\diamond$.

The increment of the Kirchhoff stress can be obtained from Equations (1) and (2) as

$$\Delta\boldsymbol{\tau} = \mathbb{C}^{\mathrm{e}} : \Delta\boldsymbol{d}^{\mathrm{e}} + \Delta\boldsymbol{\Omega}\boldsymbol{\tau}_n - \boldsymbol{\tau}_n\Delta\boldsymbol{\Omega}. \tag{77}$$

where $\Delta\boldsymbol{d}^{\mathrm{e}} = \Delta\boldsymbol{d} - \Delta\boldsymbol{d}^{\mathrm{p}}$. The substitution of Equations (70), (11), and (19) to this expression yields the following update formula for the Kirchhoff stress:

$$\boldsymbol{\tau}_{n+1} = \boldsymbol{\tau}_n + \mathbb{C}^{\mathrm{e}} : \left(\Delta\boldsymbol{d} - \Delta\boldsymbol{d}^{\mathrm{p}}\right) + \Delta\boldsymbol{\Omega}\boldsymbol{\tau}_n - \boldsymbol{\tau}_n\Delta\boldsymbol{\Omega} = \boldsymbol{\tau}_{n+1}^{\mathrm{trial}} - \sqrt{6}G\Delta\gamma^{\mathrm{p}}\frac{\boldsymbol{\eta}_{n+1}}{\left\|\boldsymbol{\eta}_{n+1}\right\|} + \Delta\boldsymbol{\Omega}\boldsymbol{\tau}_n - \boldsymbol{\tau}_n\Delta\boldsymbol{\Omega}, \tag{78}$$

where trial Kirchhoff stress has been defined as $\boldsymbol{\tau}_{n+1}^{\mathrm{trial}} := \boldsymbol{\tau}_n + \mathbb{C}^{\mathrm{e}} : \Delta\boldsymbol{d}$ and G is shear moduli of elasticity.

From Equation (16), the increment of the hardening variable for isotropic hardening is identified with the plastic multiplier as $\Delta\alpha^{\mathrm{i}} = \Delta\gamma^{\mathrm{p}}$, so that $\alpha^{\mathrm{i}}_{n+1} = \alpha^{\mathrm{i}}_n + \Delta\gamma^{\mathrm{p}}$. Then, one of the isotropic hardening functions in Equation (37) irrelevant to the memory surface is given as

$$\kappa_{\mathrm{y}}\left[\Delta\gamma^{\mathrm{p}}\right] = L_{\mathrm{y}}(\alpha^{\mathrm{i}}_n + \Delta\gamma^{\mathrm{p}}) + R_{\mathrm{y}}\left(1 - \exp\left\{-r_{\mathrm{y}}(\alpha^{\mathrm{i}}_n + \Delta\gamma^{\mathrm{p}})\right\}\right). \tag{79}$$

Similarly, the isotropic hardening function for the memory surface is a function of hardening variable α^{m} that is discretized as

$$\kappa_{\mathrm{m}}\left[\Delta\gamma^{\mathrm{p}},\ \Delta\gamma^{\mathrm{m}}\right] = L^{\mathrm{q}}_{n+1}\left[\Delta\gamma^{\mathrm{m}}\right]\left(\alpha^{\mathrm{m}}_n + \Delta\gamma^{\mathrm{p}} - \Delta\gamma^{\mathrm{m}}\right), \tag{80}$$

where we have used the relationships, $\alpha^{\mathrm{m}}_{n+1} = \alpha^{\mathrm{m}}_n + \Delta\alpha^{\mathrm{m}}$, $\Delta\alpha^{\mathrm{m}} = \Delta\gamma^{\mathrm{p}} - \Delta\gamma^{\mathrm{m}}$ and $\Delta q = \Delta\gamma^{\mathrm{m}}$, which correspond to the discretized forms of Equations (40) and (74), respectively. Here, the evolution Equation (41) of the hardening modulus is discretized in time as

$$L^{\mathrm{q}}_{n+1}\left[\Delta\gamma^{\mathrm{m}}\right] = L^{\mathrm{q}}_n + \Delta L^{\mathrm{q}}\left[\Delta\gamma^{\mathrm{m}}\right], \tag{81}$$

where

$$\Delta L^{\mathrm{q}}\left[\Delta\gamma^{\mathrm{m}}\right] = \left\{m_1(q_n + \Delta\gamma^{\mathrm{m}})^2 + m_2(q_n + \Delta\gamma^{\mathrm{m}}) + m_3\right\}\Delta\gamma^{\mathrm{m}}, \tag{82}$$

with $q_{n+1} = q_n + \Delta q = q_n + \Delta\gamma^{\mathrm{m}}$.

On the other hand, the increment of each back stress of Equation (45) is approximated as

$$\boldsymbol{\beta}^{(k)}_{n+1} - \boldsymbol{\beta}^{(k)}_n = \sqrt{\frac{3}{2}}a^{(k)}\Delta\gamma^{\mathrm{p}}\frac{\boldsymbol{\eta}_{n+1}}{\left\|\boldsymbol{\eta}_{n+1}\right\|} - b^{(k)}\Delta\gamma^{\mathrm{p}}\boldsymbol{\beta}^{(k)}_{n+1} + \Delta\boldsymbol{\Omega}\boldsymbol{\beta}^{(k)}_n - \boldsymbol{\beta}^{(k)}_n\Delta\boldsymbol{\Omega}, \tag{83}$$

which yields

$$\boldsymbol{\beta}^{(k)}_{n+1} = \frac{1}{1 + b^{(k)}\Delta\gamma^{\mathrm{p}}}\left(\boldsymbol{\beta}^{(k)}_n + \sqrt{\frac{3}{2}}a^{(k)}\Delta\gamma^{\mathrm{p}}\frac{\boldsymbol{\eta}_{n+1}}{\left\|\boldsymbol{\eta}_{n+1}\right\|} + \Delta\boldsymbol{\Omega}\boldsymbol{\beta}^{(k)}_n - \boldsymbol{\beta}^{(k)}_n\Delta\boldsymbol{\Omega}\right). \tag{84}$$

Then, the back stress in the Chaboche model (44) at T_{n+1} is expressed as

$$\boldsymbol{\beta}_{n+1} = \sum_{k=1}^{N^{\mathrm{kin}}}\boldsymbol{\beta}^{(k)}_{n+1} = \boldsymbol{B}^{\mathrm{kin}} + \sqrt{6}A^{\mathrm{kin}}\Delta\gamma^{\mathrm{p}}\frac{\boldsymbol{\eta}_{n+1}}{\left\|\boldsymbol{\eta}_{n+1}\right\|}, \tag{85}$$

where we have defined

$$\boldsymbol{B}^{\mathrm{kin}} := \sum_{k=1}^{N^{\mathrm{kin}}}\frac{\boldsymbol{\beta}^{(k)}_n + \Delta\boldsymbol{\Omega}\boldsymbol{\beta}^{(k)}_n - \boldsymbol{\beta}^{(k)}_n\Delta\boldsymbol{\Omega}}{1 + b^{(k)}\Delta\gamma^{\mathrm{p}}} \qquad A^{\mathrm{kin}} := \frac{1}{2}\sum_{k=1}^{N^{\mathrm{kin}}}\frac{a^{(k)}}{1 + b^{(k)}\Delta\gamma^{\mathrm{p}}}. \tag{86}$$

Accordingly, the substitution of Equations (78) and (85) into Equation (12) yields the following expression of the relative stress:

$$\boldsymbol{\eta}_{n+1} = \boldsymbol{\tau}_{\mathrm{d},\ n+1} - \boldsymbol{\beta}_{n+1} = \boldsymbol{\tau}^{\mathrm{trial}}_{\mathrm{d},\ n+1} - \boldsymbol{B}^{\mathrm{kin}} - \sqrt{6}\left(G + A^{\mathrm{kin}}\right)\Delta\gamma^{\mathrm{p}}\frac{\boldsymbol{\eta}_{n+1}}{\left\|\boldsymbol{\eta}_{n+1}\right\|}. \tag{87}$$

Taking the norm of the $\boldsymbol{\eta}$ on both side, we have

$$\left\|\boldsymbol{\eta}_{n+1}\right\| = \left\|\boldsymbol{\tau}^{\mathrm{trial}}_{\mathrm{d},\ n+1} - \boldsymbol{B}^{\mathrm{kin}}\right\| - \sqrt{6}\left(G + A^{\mathrm{kin}}\right)\Delta\gamma^{\mathrm{p}}, \tag{88}$$

from which Equation (11) yields the following return mapping equation:

$$r_1\left[\Delta\gamma^{\mathrm{p}},\ \Delta\gamma^{\mathrm{m}}\right] := \frac{1}{G}\Phi^{\mathrm{p}} = \frac{1}{G}\left\{\sqrt{\frac{3}{2}}\left\|\boldsymbol{\tau}^{\mathrm{trial}}_{\mathrm{d},\ n+1} - \boldsymbol{B}^{\mathrm{kin}}\right\| - 3\left(G + A^{\mathrm{kin}}\right)\Delta\gamma^{\mathrm{p}} - \sigma_{\mathrm{y}}\left[\Delta\gamma^{\mathrm{p}},\ \Delta\gamma^{\mathrm{m}}\right]\right\} = 0. \tag{89}$$

Here, Equation (36) has been used along with Equations (79) and (80) to obtain

$$\sigma_y\left[\Delta\gamma^{\mathrm{p}},\ \Delta\gamma^{\mathrm{m}}\right] = \sigma_{\mathrm{y0}} + \kappa_{\mathrm{y}}\left[\Delta\gamma^{\mathrm{p}}\right] + \kappa_{\mathrm{m}}\left[\Delta\gamma^{\mathrm{p}},\ \Delta\gamma^{\mathrm{m}}\right]. \tag{90}$$

Meanwhile, replacing $\Phi^{\mathrm{m}}_{\sigma}$ in Equation (75) by $\Phi^{\mathrm{m}}_{\varepsilon}$ whose specific form was provided in Equation (33), we discretize the resulting equation as

$$r_2\left[\Delta\gamma^{\mathrm{p}},\ \Delta\gamma^{\mathrm{m}},\ s_{2,\ n+1}\right] := \Phi^{\mathrm{m}}_{\varepsilon} + s^2_{2,\ n+1} = \sqrt{\frac{2}{3}}\left\|\boldsymbol{\varepsilon}^{\mathrm{p}}_n + \Delta\gamma^{\mathrm{p}}\boldsymbol{N}^{\mathrm{p}}\right\| - \left(q_n + \Delta\gamma^{\mathrm{m}}\right) + s^2_{2,\ n+1} = 0. \tag{91}$$

where the relationships $\boldsymbol{\varepsilon}^{\mathrm{p}}_{n+1} = \boldsymbol{\varepsilon}^{\mathrm{p}}_n + \Delta\gamma^{\mathrm{p}}\boldsymbol{N}^{\mathrm{p}}$ and $q_{n+1} = q_n + \Delta\gamma^{\mathrm{m}}$ have been used. Also, the time discretization of Equation (76) is simply given as

$$r_3\left[\Delta\gamma^{\mathrm{m}},\ s_{2,\ n+1}\right] := \Delta\gamma^{\mathrm{m}}s^2_{2,\ n+1} - \mu_2 = 0. \tag{92}$$

Finally, Equations (89), (91), and (92) constitute a set of simultaneous nonlinear equations to be iteratively solved for $\Delta\gamma^{\mathrm{p}}$, $\Delta\gamma^{\mathrm{m}}$, and s_2 by Newton method as

$$\begin{bmatrix} \frac{\partial r_1}{\partial\Delta\gamma^{\mathrm{p}}} & \frac{\partial r_1}{\partial\Delta\gamma^{\mathrm{m}}} & \frac{\partial r_1}{\partial s_2} \\ \frac{\partial r_2}{\partial\Delta\gamma^{\mathrm{p}}} & \frac{\partial r_2}{\partial\Delta\gamma^{\mathrm{m}}} & \frac{\partial r_2}{\partial s_2} \\ \frac{\partial r_3}{\partial\Delta\gamma^{\mathrm{p}}} & \frac{\partial r_3}{\partial\Delta\gamma^{\mathrm{m}}} & \frac{\partial r_3}{\partial s_2} \end{bmatrix}\begin{Bmatrix} \delta\Delta\gamma^{\mathrm{p}} \\ \delta\Delta\gamma^{\mathrm{m}} \\ \delta s_2 \end{Bmatrix} = -\begin{Bmatrix} r_1 \\ r_2 \\ r_3 \end{Bmatrix}, \tag{93}$$

where $\delta\bullet$ is a corrector of $\bullet$. Here, the nonzero components of the Jacobian matrix are given as

$$\frac{\partial r_1}{\partial\Delta\gamma^{\mathrm{p}}} = -\frac{1}{G}\left\{\frac{\partial\boldsymbol{B}^{\mathrm{kin}}}{\partial\Delta\gamma^{\mathrm{p}}} : \boldsymbol{N}^{\mathrm{p}} + 3\left(G + A^{\mathrm{kin}} + \Delta\gamma^{\mathrm{p}}\frac{\partial A^{\mathrm{kin}}}{\partial\Delta\gamma^{\mathrm{p}}}\right) + \frac{\partial\sigma_y}{\partial\Delta\gamma^{\mathrm{p}}}\right\}, \tag{94}$$

$$\frac{\partial r_1}{\partial\Delta\gamma^{\mathrm{m}}} = \frac{1}{G}\left\{\frac{\partial L^{\mathrm{q}}}{\partial\Delta\gamma^{\mathrm{m}}}\left(\Delta\gamma^{\mathrm{p}} - \Delta\gamma^{\mathrm{m}}\right) - L^{\mathrm{q}}\right\}, \tag{95}$$

$$\frac{\partial r_2}{\partial\Delta\gamma^{\mathrm{p}}} = \sqrt{\frac{2}{3}}\overline{\boldsymbol{N}}^{\mathrm{m}} : \left(\boldsymbol{N}^{\mathrm{p}} + \Delta\gamma^{\mathrm{p}}\frac{\partial\boldsymbol{N}^{\mathrm{p}}}{\partial\Delta\gamma^{\mathrm{p}}}\right), \quad \frac{\partial r_2}{\partial\Delta\gamma^{\mathrm{m}}} = -1, \quad \frac{\partial r_2}{\partial s_2} = 2s_2, \tag{96}$$

$$\frac{\partial r_3}{\partial\Delta\gamma^{\mathrm{m}}} = s^2_2, \quad \frac{\partial r_3}{\partial s_2} = 2s_2\Delta\gamma^{\mathrm{m}}, \tag{97}$$

where

$$\frac{\partial\boldsymbol{B}^{\mathrm{kin}}}{\partial\Delta\gamma^{\mathrm{p}}} = -\sum_{k=1}^{N^{\mathrm{kin}}}\frac{b^{(k)}\left(\boldsymbol{\beta}^{(k)}_n + \Delta\boldsymbol{\Omega}\boldsymbol{\beta}^{(k)}_n - \boldsymbol{\beta}^{(k)}_n\Delta\boldsymbol{\Omega}\right)}{\left(1 + b^{(k)}\Delta\gamma^{\mathrm{p}}\right)^2}. \tag{98}$$

$$\frac{\partial A^{\mathrm{kin}}}{\partial\Delta\gamma^{\mathrm{p}}} = -\frac{1}{2}\sum_{k=1}^{N^{\mathrm{kin}}}\frac{a^{(k)}b^{(k)}}{\left(1 + b^{(k)}\Delta\gamma^{\mathrm{p}}\right)^2}. \tag{99}$$

$$\frac{\partial\sigma_{\mathrm{y}}}{\partial\Delta\gamma^{\mathrm{p}}} = L_{\mathrm{y}} + R_{\mathrm{y}}r_{\mathrm{y}}\exp\left\{-r_{\mathrm{y}}(\alpha^{\mathrm{i}}_n + \Delta\gamma^{\mathrm{p}})\right\}. \tag{100}$$

$$\frac{\partial L^{\mathrm{q}}}{\partial\Delta\gamma^{\mathrm{m}}} = m_3 + m_2(q_n + \Delta\gamma^{\mathrm{m}}) + m_1(q_n + \Delta\gamma^{\mathrm{m}})^2 + \Delta\gamma^{\mathrm{m}}\left(m_2 + 2m_1(q_n + \Delta\gamma^{\mathrm{m}})\right). \tag{101}$$

$$\frac{\partial\boldsymbol{N}^{\mathrm{p}}}{\partial\Delta\gamma^{\mathrm{p}}} = -\sqrt{\frac{3}{2}}\frac{1}{\left\|\boldsymbol{\tau}^{\mathrm{trial}}_{\mathrm{d},\ n+1} - \boldsymbol{B}^{\mathrm{kin}}\right\|}\frac{\partial\boldsymbol{B}^{\mathrm{kin}}}{\partial\Delta\gamma^{\mathrm{p}}} : \left(\boldsymbol{I}\otimes\boldsymbol{I} - \overline{\boldsymbol{N}}^{\mathrm{p}}\otimes\overline{\boldsymbol{N}}^{\mathrm{p}}\right). \tag{102}$$

When Newton method is applied to solve the global equilibrium equation, the consistent tangent moduli are needed to achieve preferable convergence performance, which can be expressed as

$$\frac{\mathrm{d}\Delta\boldsymbol{\tau}}{\mathrm{d}\Delta\boldsymbol{d}} = \mathbb{C}^{\mathrm{e}} : \left\{ \mathbb{I} - \frac{\partial \Delta\gamma^{\mathrm{p}}}{\partial \Delta\boldsymbol{d}} \otimes \left(\boldsymbol{N}^{\mathrm{p}} + \Delta\gamma^{\mathrm{p}} \frac{\partial \boldsymbol{N}^{\mathrm{p}}}{\partial \Delta\gamma^{\mathrm{p}}} \right) \right\}, \tag{103}$$

where $\mathbb{I}$ is the fourth-order identity tensor. Also, the partial differential of $\Delta\gamma^{\mathrm{p}}$ by $\Delta\boldsymbol{d}$ is represented as

$$\frac{\partial \Delta\gamma^{\mathrm{p}}}{\partial \Delta\boldsymbol{d}} = -\left(\frac{\partial r_1}{\partial \Delta\gamma^{\mathrm{p}}} \right)^{-1} \frac{\mathrm{d}\boldsymbol{r}_1}{\mathrm{d}\Delta\boldsymbol{d}} = -2G \left(\frac{\partial r_1}{\partial \Delta\gamma^{\mathrm{p}}} \right)^{-1} \boldsymbol{N}^{\mathrm{p}}, \tag{104}$$

which has been simplified because of $\mathrm{d}r_2/\mathrm{d}\Delta\boldsymbol{d} = \mathrm{d}r_3/\mathrm{d}\Delta\boldsymbol{d} = 0$. The partial differential of $\boldsymbol{N}^{\mathrm{p}}$ by $\Delta\gamma^{\mathrm{p}}$ in Equation (103) has already provided as Equation (102). Here, it should be noted that the normal vector on the yield surface is expressed as a function of $\Delta\gamma^{\mathrm{p}}$:

$$\boldsymbol{N}^{\mathrm{p}}\left[\Delta\gamma^{\mathrm{p}}\right] = \sqrt{\frac{3}{2}} \frac{\boldsymbol{\eta}_{n+1}}{\left\|\boldsymbol{\eta}_{n+1}\right\|} = \sqrt{\frac{3}{2}} \frac{\boldsymbol{\tau}^{\mathrm{trial}}_{\mathrm{d},\, n+1} - \boldsymbol{B}^{\mathrm{kin}}\left[\Delta\gamma^{\mathrm{p}}\right]}{\left\| \boldsymbol{\tau}^{\mathrm{trial}}_{\mathrm{d},\, n+1} - \boldsymbol{B}^{\mathrm{kin}}\left[\Delta\gamma^{\mathrm{p}}\right] \right\|}, \tag{105}$$

which can be easily obtained from the substitution of Equation (88) into Equation (87).

4.2 | Numerical algorithm

An efficient numerical algorithm by the combined use of the conventional return mapping method and PDIPM is established as follows:

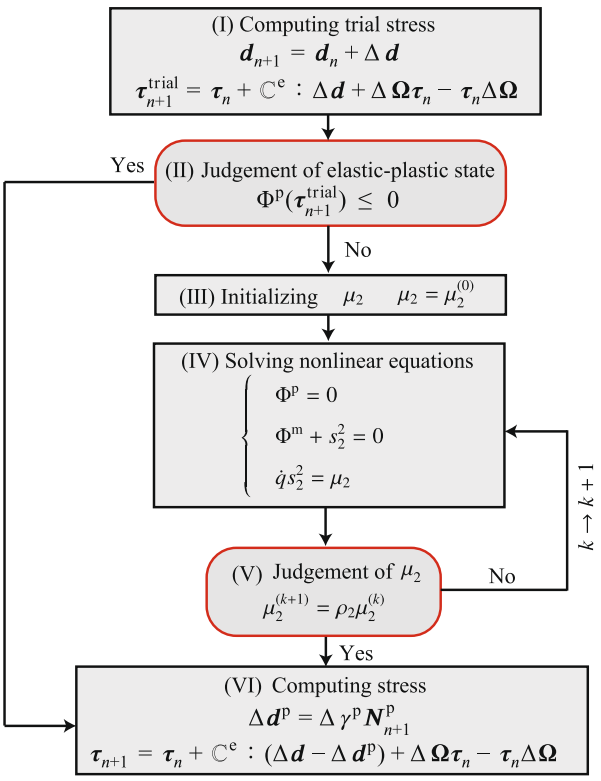

FIGURE 2 Flowchart of hybrid implicit stress update algorithm combined between primal-dual interior point method and return mapping algorithm for a hypoelastic-plastic model with memory surface

(I) Given the strain increment $\Delta \boldsymbol{d}$, compute the trial stress $\boldsymbol{\tau}_{n+1}^{\text{trial}}$ on the assumption that $\Delta\gamma^{\text{p}} = 0$.
(II) Judge loading or unloading state from Equation (89) with trial stress $\boldsymbol{\tau}_{n+1}^{\text{trial}}$ being input. If the left-hand side of Equation (89) is less than zero, skips to Step (VI). Otherwise, go to the next step.
(III) Set the duality gap μ_2 at the initial value of $\mu_2^{(k)}$ where $k = 0$.
(IV) Solve Equations (89), (91), and (92) for $\Delta\gamma^{\text{p}}$, $\Delta\gamma^{\text{m}}$ and s_2 by Newton method.
(V) When the duality gap $\mu_2^{(k)}$ becomes smaller than tolerance ϵ, go to the next step. Otherwise, setting the counter to be $k \to k+1$, update μ_2 by the path-following method as

$$\mu_2^{(k+1)} = \rho_2 \, \mu_2^{(k)}, \tag{106}$$

where ρ_2 is a constant value between 0 and 1. Then, go back to Step (IV).
(VI) Update the stress and all the internal state variables.

For more detail, the flowchart of hybrid implicit stress update algorithm is summarized in Figure 2.

5 | NUMERICAL EXAMPLES

Several numerical examples are presented to demonstrate the capability of our hybrid implicit stress update algorithm. After confirming the applicability of the PDIPM to elastic-plastic models with isotropic and/or kinematic hardening rules, we verify the performance of the proposed hybrid algorithm in updating stress for the elastic-plastic model with memory surface.

5.1 | Numerical accuracy and convergence of the PDIPM

Before demonstrating the performance of the proposed hybrid algorithm for implicit stress update, we examine the numerical accuracy and convergence property of the PDIPM applied to an elastic-plastic model with isotropic hardening.

An iso-error map[31] is employed as a measure of accuracy in stress update. To obtain an iso-error map within time interval $[T_n, T_{n+1}]$, we first specify a certain state of stress $\boldsymbol{\tau}_n$ satisfying the yield condition at time T_n and prepare various states of trial stress $\boldsymbol{\tau}_{n+1}^{\text{trial}}$ at time T_{n+1} by giving various strain increments determined by $\boldsymbol{e}_{\text{T}}$ and $\boldsymbol{e}_{\text{N}}$ as

$$\boldsymbol{\tau}_{n+1}^{\text{trial}} = \boldsymbol{\tau}_n + \frac{\Delta\tau_{\text{T}}}{\tau_{\text{eq},\,n}}\boldsymbol{e}_{\text{T}} + \frac{\Delta\tau_{\text{N}}}{\tau_{\text{eq},\,n}}\boldsymbol{e}_{\text{N}}, \tag{107}$$

where $\boldsymbol{e}$ is the outward unit "vector" on the yield surface, $\bullet_{\text{T}}$ and $\bullet_{\text{N}}$ are the tangential and normal components of $\bullet$, respectively, and $\tau_{\text{eq},\,n}$ is the von-Mises equivalent stress computed from $\boldsymbol{\tau}_n$. Then, a stress update method of interest is applied to obtain the current stress state $\boldsymbol{\tau}^{\text{num}} \equiv \boldsymbol{\tau}_{n+1}$ and calculate the error by the following formula:

$$\epsilon_{\text{error}} = \frac{||\boldsymbol{\tau}^{\text{exact}} - \boldsymbol{\tau}^{\text{num}}||}{||\boldsymbol{\tau}^{\text{exact}}||}, \tag{108}$$

where $\boldsymbol{\tau}^{\text{exact}}$ is the reference solution incrementally obtained for sufficiently small increments of strain. In this study, each small increment is equally set at one-thousandth of the given strain increment.

The conventional elastic-plastic model with the isotropic hardening rule is employed for the sake of simplicity, while kinematic hardening is not considered. The material parameters are given in Table 1. A unidirectional loading is applied, and the specified stress $\boldsymbol{\tau}_n$ satisfying the yield condition at time T_n is when the von-Mises stress reaches 350 MPa. In this particular example, the duality gap is initially set at a sufficiently small value 1.0×10^{-8} so that its update in the path-following method needs not be made. Figure 3 shows the obtained iso-error maps for the conventional return mapping algorithm and the PDIPM presented in Section 3.1. As can be seen from this figure, the maximum value of numerical error of the PDIPM is equivalent to that of the return mapping algorithm, and the distributions of numerical errors appear identical to each other.

Figure 4 shows the number of Newton's iterations of the return mapping algorithm and the PDIPM when the above iso-error maps are obtained. As can be seen from Figure 4A, the maximum number of Newton's iterations was at most

TABLE 1 Material constants to obtain iso-error maps

Young's modulus	Poisson's ratio	Initial yield stress	Isotropic hardening		
E (GPa)	ν	σ_{y0} (MPa)	L_y (MPa)	R_y (MPa)	r_y
206.0	0.3	300.0	1000.0	500.0	20.0

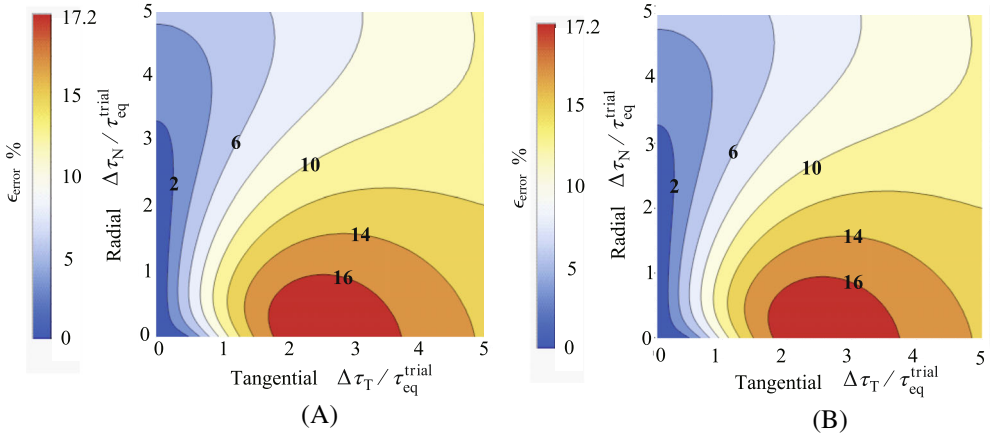

FIGURE 3 Iso-error maps obtained by return mapping algorithm and primal-dual interior method. (A) Return mapping algorithm; (B) Primal-dual interior point method

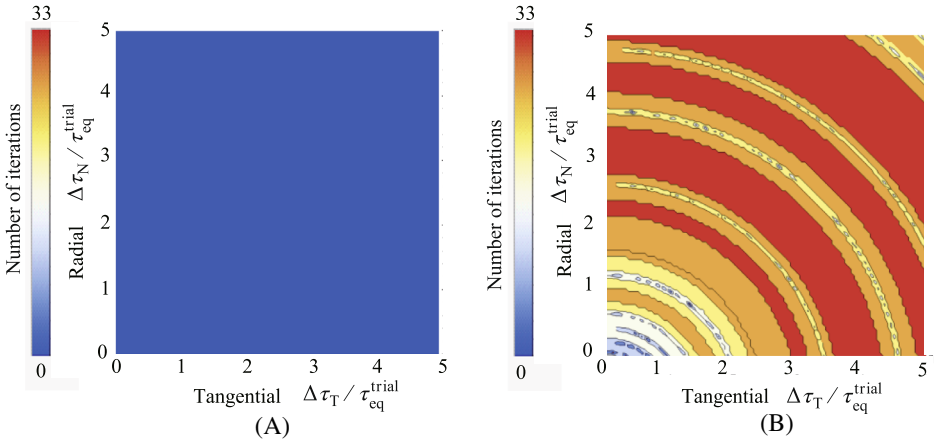

FIGURE 4 Number of Newton's iterations to obtain iso-error maps by return mapping algorithm and primal-dual interior method. (A) Return mapping algorithm; (B) Primal-dual interior point method

four times for the return mapping algorithm, although the color levels are not well identified. On the other hand, from Figure 4B, the maximum number of iteration was 33 times for the PDIPM, since Equations (56) and (57) were simultaneously solved by Newton method. Thus, as pointed out in Section 3.2, the convergence property of the PDIPM tends to be inferior to that of the conventional return mapping algorithm. However, as will be demonstrated later, when a class of elastic-plastic models with memory surface is adopted, the standard implicit stress update often does not work, and the combination of the return mapping algorithm and the PDIPM must be effective.

5.2 | Round bar with notch under cyclic loading with different ranges of plastic strain

Targeting a notched round steel bar under cyclic loading with different amplitudes, we verify the performance of the proposed hybrid stress update scheme for a hypoelastic-plastic constitutive law with memory surface. The specimen used in

this numerical simulation is schematized in Figure 5 with the spatial dimensions. Figure 6 shows the FE model generated with eight-node quadrilateral axisymmetric elements in consideration of the geometry and the schematized boundary condition. The material constants are provided in Table 2. The number of divided back stresses is set at $N^{\mathrm{kin}} = 2$. The initial value for the following-path method are set at $\mu_2^{(0)} = 1.0 \times 10^{-5}$ with $\rho_2 = 1.0 \times 10^{-1}$, and the tolerance to judge the convergence is set at $\epsilon = 1.0 \times 10^{-8}$.

First, the convergence properties of the proposed hybrid algorithm and the conventional return mapping method are compared at the onset of plastic deformation in the notched round bar under tensile loading. Figure 7 shows the change of residual errors in the Newton iterative process evaluated at the Gauss quadrature point closest to the center of the specimen, which is indicated by ① in Figure 6. Here, the vertical axis is the natural logarithmic scale. As can be seen from Figure 7, the return mapping algorithm does not attain convergence. More specifically, after the residual error of the return mapping algorithm decreases to a certain value, it does not get any smaller. This is because the residual error oscillates between positive and negative values in the Newton's iteration due to the branch condition associated with the inequality constraint for the memory surface. On the other hand, the proposed hybrid algorithm can obtain the converged

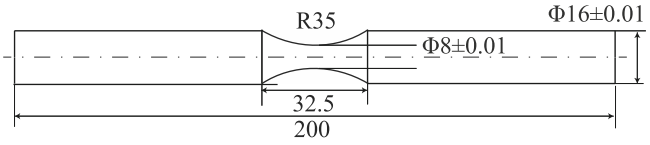

FIGURE 5 Geometry of a notched round bar with notch

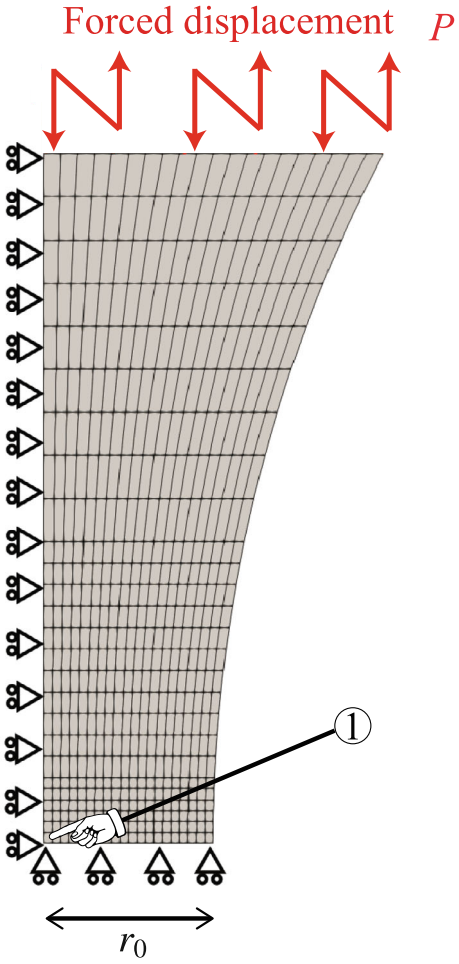

FIGURE 6 Finite element model of a notched round bar with notch and boundary conditions

TABLE 2 Material constants of a notched round bar with notch

Young's modulus	Poisson's ratio	Initial yield stress	Isotropic hardening		
E (GPa)	ν	σ_{y0} (MPa)	L_y (MPa)	R_y (MPa)	r_y
206.0	0.3	300.0	0.0	80.0	5.0

Kinematic hardening				Additional hardening with memory surface		
a_1	b_1	a_2	b_2	m_1 (MPa)	m_2 (MPa)	m_3 (MPa)
10,000.0	100.0	290.0	0.01	8663.5	−27.5	0.0

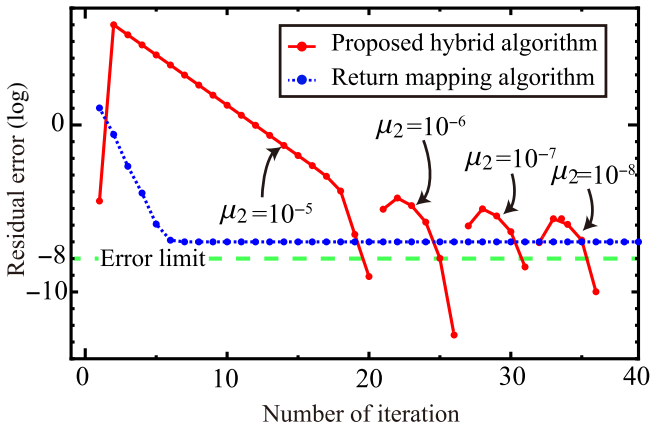

FIGURE 7 Change of residual error by iterative computation of proposed hybrid algorithm and return mapping algorithm

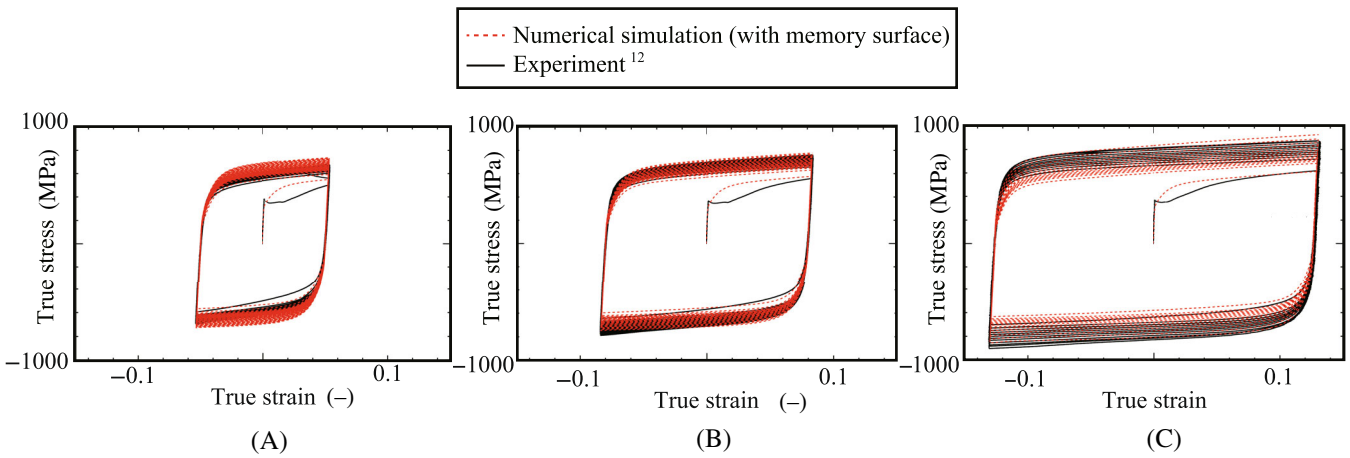

FIGURE 8 Relationship between stress and strain obtained by hypoelastic-plastic model with memory surface using proposed hybrid algorithm. (A) $\Delta\epsilon^p = 0.05$; (B) $\Delta\epsilon^p = 0.08$; (C) $\Delta\epsilon^p = 0.126$

solution in each Newton's iterative process with different duality gaps, although the residual error temporarily increases right after the duality gap update in the path-following scheme for the PDIPM. As a result, the proposed hybrid algorithm is able to realize that the residual error finally becomes smaller than $\epsilon = 1.0 \times 10^{-8}$.

Second, we consider cyclic loading with different plastic strain amplitudes: $\Delta\varepsilon_a^p = 0.05$, 0.08 and 0.126. Figure 8 shows the stress-strain curves obtained by the finite element analysis with the proposed stress update scheme. In this figure, the experimental results,[12] which were obtained by the experiments conducted in accordance with Japan Welding Engineering Society Standard WES-162, are also included. Here, the true stress and strain are defined as, respectively,

$$\sigma_a = \frac{P}{\pi r^2}, \tag{109}$$

$$\varepsilon_a = -2 \ln \frac{r}{r_0}, \tag{110}$$

where P is the axial load calculated as the summation of nodal forces at the top surface of the specimen, r is the radius of the minimum cross-section and r_0 is its initial value. It can be confirmed from these figures that the simulated curves obtained with the hypoelastic-plastic model with memory surface are qualitatively in close agreement with the experimental ones. It should be noted here that the application of the conventional return mapping method did not work for this problem.

As a reference, the stress-strain curves obtained with the standard hypoelastic-plastic model without memory surface are shown in Figure 9, for which the material constants in Table 2 have been used. As can be seen from Figure 9A, the simulated stress-strain curve for plastic strain range $\Delta\varepsilon_a^p = 0.05$ fairly fits with the experimental one. However, as shown in Figure 9B,C, the other two curves for plastic strain ranges $\Delta\varepsilon_a^p = 0.08$ and 0.126 deviate from the experimental ones. This discrepancy is due to the fact that the standard model is incapable of representing the change of hardening behavior with the increase in plastic strain ranges and as a result underestimates the stress responses as compared to the experimental results. Therefore, the hypoelastic-plastic model with the hardening rule depending on the memory surface enables us to properly simulate the mechanical behavior of a notched round bar under cyclic loading with different plastic

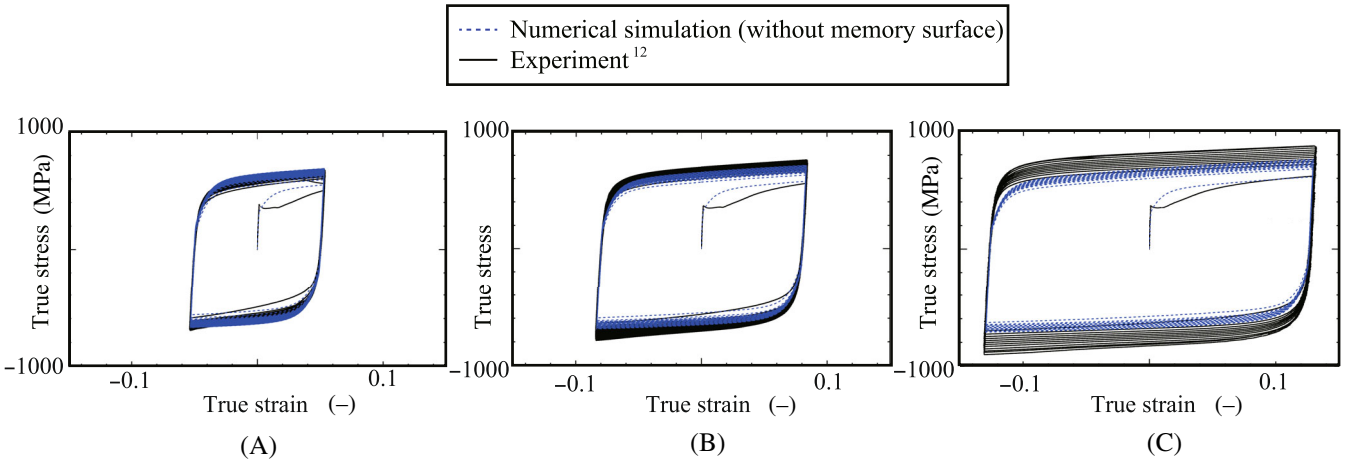

FIGURE 9 Relationship between stress and strain obtained by hypoelastic-plastic model without memory surface using return mapping algorithm. (A) $\Delta\epsilon^p = 0.05$; (B) $\Delta\epsilon^p = 0.08$; (C) $\Delta\epsilon^p = 0.126$

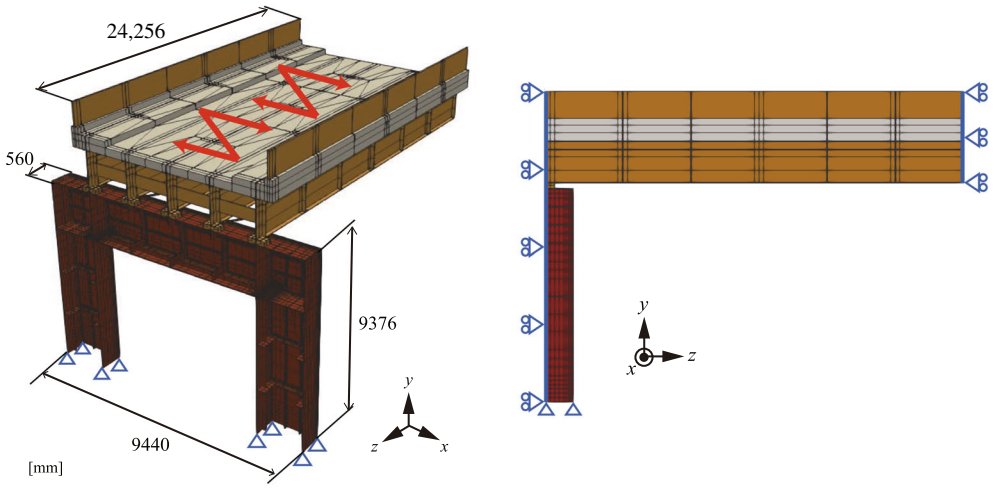

FIGURE 10 Finite element model of steel bridge with spatial dimensions and boundary conditions

strain ranges. Thanks to the extension of the hybrid stress update method to the framework of finite strain theory, the stress-strain curves are better predicted than those obtained in our previous study.[29] Yet, because of the proposed hybrid stress update method, the calculations could have been stably and efficiently performed.

5.3 | Steel bridge subjected to seismic loading

The last example targets a steel bridge subjected to a seismic load during earthquake, which inevitably necessitates the hardening rule with memory surface. Indeed, the ex-post yield strength in regions which exhibit severe plastic deformation must be elaborately predicted to estimate the residual load bearing ability of the bridge after the earthquake.

The finite element model of the steel bridge is shown in Figure 10 with the representative sizes. Loading and support conditions are also roughly depicted. Here, the symmetry condition is considered in the *x*-*y* plane, and the bottom of each bridge pier is fixed in all directions. As shown in Figure 11, different colors are used to indicate the material models for the bridge pier, floor slab, and the others, in which the adopted constitutive models with material constants are also provided. In the attached table, "Memory surface" is the same material model and parameters used in the previous example, and "Noe-Hookean" implies that the material is assumed to follow the standard neo-Hookean hyperelastic model and not to deform plastically. A simple acceleration wave is assumed to be caused by an earthquake as shown in Figure 12. Here, the amplitude of the wave increases for 1 s from the beginning and then remains constant for 2 s, and the frequency is set at 8.93 Hz.

Figure 13 shows the distributions of accumulated plastic strain at 1.0, 2.0 and 3.0 s. It can be seen from these figures that the plastic deformation concentrates around the corners of intersection and the bottom side of each bridge pier, and the accumulated plastic strain gradually increases with time even after 1 s, reflecting the assumed hardening characteristics. Also, to investigate differences in material behavior by location, we choose Points ② and ③ indicated in Figure 13C and

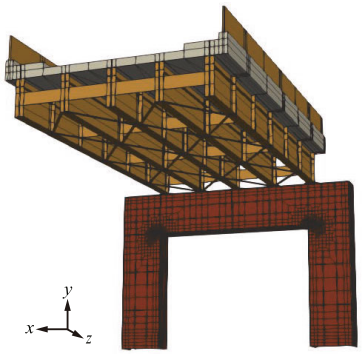

	Material model	Mass density [kg/m³]	Young's moduius [GPa]	Poisson's ratio
	Memory surface	7.9×10^{-3}	206.0	0.3
	Neo-Hookean	$7.9 \quad 10^{-3}$	206.0	0.3
	Neo-Hookean	2.4×10^{-3}	206.0	0.3

FIGURE 11 Material models and mass densities corresponding to different colored parts of steel bridge

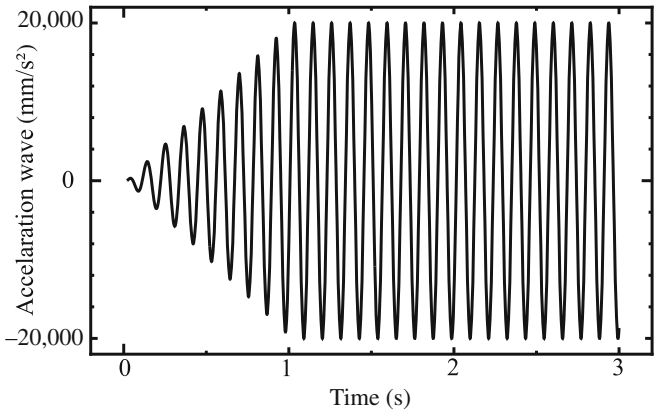

FIGURE 12 Acceleration wave caused by earthquake

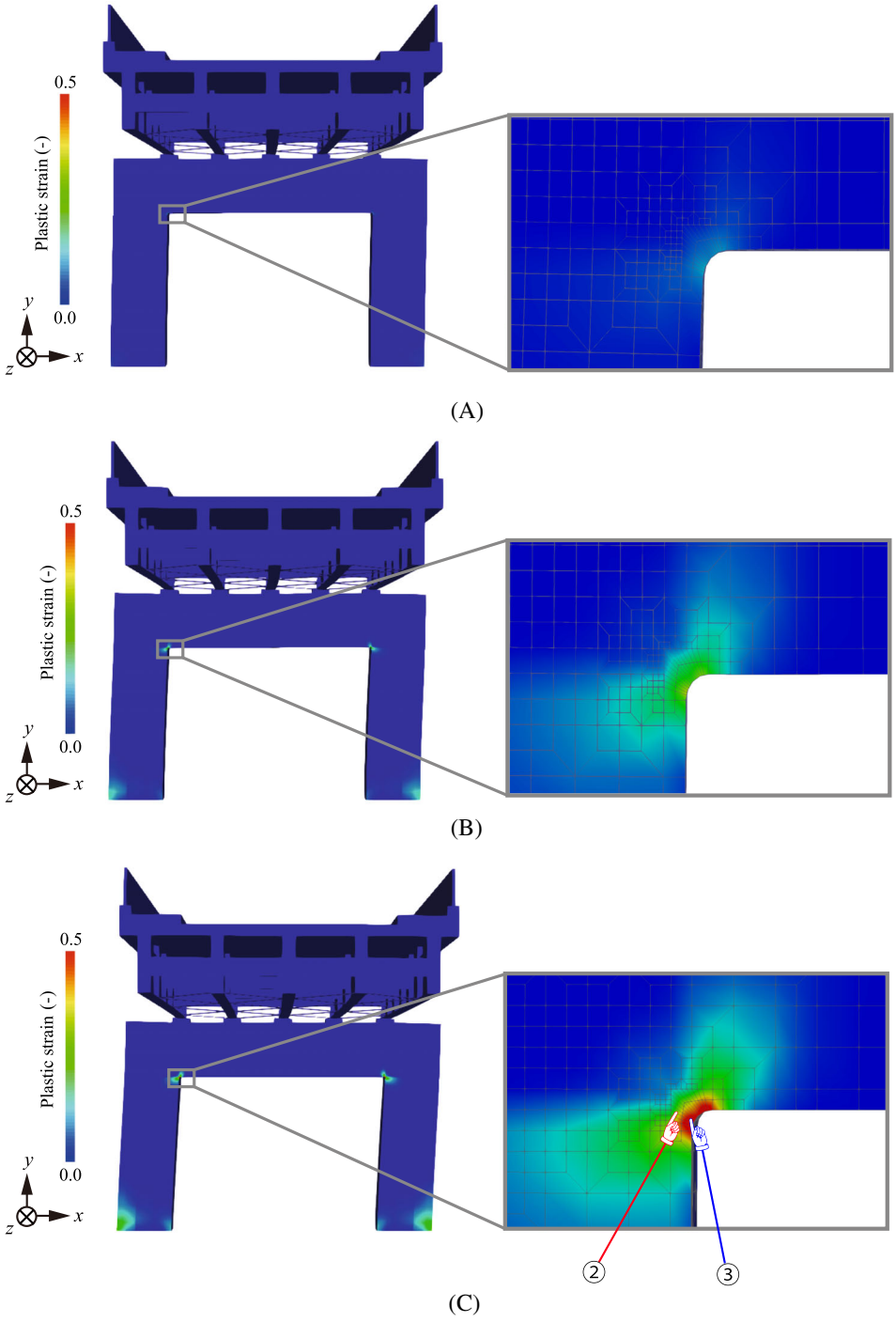

FIGURE 13 Variation of accumulated plastic strains with time. (A) 1.0 s; (B) 2.0 s; (C) 3.0 s

compare the corresponding stress-plastic strain curves as shown in Figure 14. Here, each of the *xy* shear components has been selected as a representative. As can be seen from these graphs, the plastic ranges are different by location reflecting the difference in stress concentration. It is, however, more pertinent to note that the slope of the hardening curve for Point ③ is greater than that of ②. This manifests the characteristics of the memory surface that determine the degree of hardening. Thus, the hypoelastic-plastic model with the hardening rule depending on the memory surface is inevitable to properly predict the structural behavior of this kind of engineering structures subjected to cyclic loading. Considering the fact that the standard return mapping algorithm is useless for this material model, we conclude that the proposed hybrid algorithm is essential for reliable and stable stress update in an efficient manner.

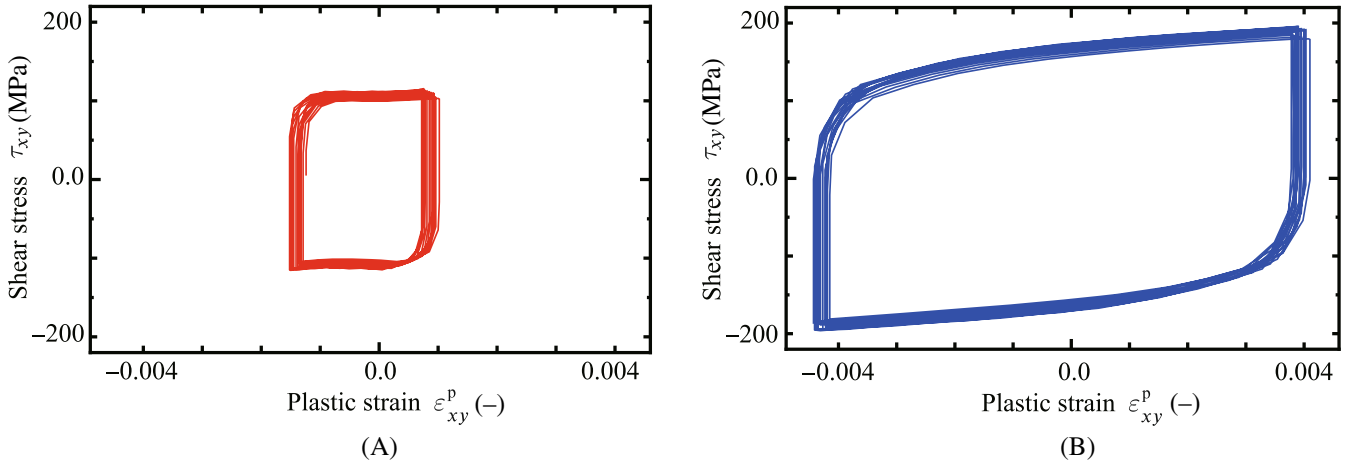

FIGURE 14 Relationship between shear stress and plastic strain at different locations. (A) Point ②; (B) Point ③

6 | CONCLUSIONS

To perform the implicit stress update for a class of hypoelastic-plastic models with the hardening rule depending on the memory surface, we have proposed a hybrid strategy by the blend of the standard return mapping algorithm and the PDIPM. Since the PDIPM requires an additional iterative procedure to perform stress update by the application of the path following method, there is no room for this method when only a single constraint condition is involved in the optimization problem relevant to a conventional elastic-plastic model. In fact, as demonstrated in the first numerical example, the convergence property of the PDIPM for the J^2 plasticity frequently used for its simplicity is of no utility to that of the return mapping algorithm, although their numerical accuracies are almost identical. However, when we are concerned with advanced elastic-plastic constitutive laws such as a class of hypoelastic-plastic models with memory surface, the conventional return mapping algorithm is useless, and the PDIPM comes into its own. That is, the proposed hybrid algorithm enables us to smoothly and stably obtain the set of solutions of a minimization problem with coupled inequality constraints associated with yield and memory surfaces as demonstrated in the second and third numerical examples. In conclusion, the combination of the return mapping algorithm and the PDIPM could be an effective tool for advanced elastic-plastic models.

However, we should mention that the formulation presented in this study is not free from flaws. Indeed, the correspondence between the hypoelastic-plastic model with memory surface and the relevant optimization problem has not been rigorously assured, because the transformation of the memory surface in the stress space into that in the strain space is not trivial. A similar argument is made for the nonassociative hardening rule such as the Chaboche model that may deviate from the principle of maximum dissipation. Nevertheless, the somewhat heuristic derivation of the numerical algorithm presented in this study has worked well in the implicit stress update for the adopted advanced elastic-plastic model.

ACKNOWLEDGMENTS
This work was supported by JSPS KAKENHI Grant Numbers JP22H03602.

CONFLICT OF INTEREST
The authors declare no potential conflict of interests.

DATA AVAILABILITY STATEMENT
The data that support the findings of this study are available from the corresponding author upon reasonable request.

ORCID
Yuichi Shintaku https://orcid.org/0000-0003-0721-8355
Kenjiro Terada https://orcid.org/0000-0001-6799-2233

REFERENCES

1. Jiang C, Hanji T, Tateishi K, Shimizu M. Local strain-based low-cycle fatigue assessment of joint structure in steel truss bridges during earthquakes. *Int J Steel Struct*. 2020;20(5):1651-1662.
2. Coffin L. A study of the effects of cyclic thermal stresses on a ductile metal. *Trans ASME*. 1954;76:931-950.
3. Manson S. *Behavior of Materials Under Conditions of Thermal Stress*. NACA; 1953:2933.
4. Armstrong P, Frederick C. A mathematical representation of the multiaxial Bauschinger effect. Technical Report RD/B/N731, CEGB; Central Electricity Generating Board, Berkeley, UK; 1966.
5. Prager W. Recent developments in the mathematical theory of plasticity. *J Appl Phys*. 1949;20(3):235-241.
6. Chaboche J, Van K, Cordier G. Modelization of the strain memory effect on the cyclic hardening of 316 stainless steel. IASMiRT; 1979.
7. Chaboche J, Rousselier G. On the plastic and viscoplastic constitutive equations-Part I: rules developed with internal variable concept. *J Press Vessel Technol*. 1983;105:153-158.
8. Chaboche J, Rousselier G. On the plastic and viscoplastic constitutive equations-Part II: application of internal variable concepts to the 316 stainless steel. *J Press Vessel Technol*. 1983;105:159-164.
9. Chaboche J. On some modifications of kinematic hardening to improve the description of ratchetting effects. *Int J Plast*. 1991;7(7):661-678.
10. Ohno N, Wang J. Kinematic hardening rules with critical state of dynamic recovery. Part I: formulation and basic features for ratchetting behavior. *Int J Plast*. 1993;9(3):375-390.
11. Ohno N, Wang J. Kinematic hardening rules with critical state of dynamic recovery. Part II: application to experiments of ratchetting behavior. *Int J Plast*. 1993;9(3):391-403.
12. Shintaku Y, Soejima K, Tsutsumi S, Terada K. An elastic-plastic constitutive law embedding cohesive cracks with plasticity-induced damage to realize degradation of strength and toughness under cyclic loading. *Tetsu-to-Hagane*. 2020;106(9):662-671. doi:10.2355/tetsutohagane.TETSU-2019-121
13. Ohno N. A constitutive model of cyclic plasticity with a nonhardening strain region. *J Appl Mech*. 1982;49(4):721-727.
14. Nouailhas D, Cailletaud G, Policella H, et al. On the description of cyclic hardening and initial cold working. *Eng Fract Mech*. 1985;21(4):887-895.
15. Chaboche J, Gaubert A, Kanouté P, Longuet A, Azzouz F, Mazière M. Viscoplastic constitutive equations of combustion chamber materials including cyclic hardening and dynamic strain aging. *Int J Plast*. 2013;46:1-22.
16. Lee C, Van Do V, Chang K. Analysis of uniaxial ratcheting behavior and cyclic mean stress relaxation of a duplex stainless steel. *Int J Plast*. 2014;62:17-33.
17. Xu L, Nie X, Fan J, Tao M, Ding R. Cyclic hardening and softening behavior of the low yield point steel BLY160: experimental response and constitutive modeling. *Int J Plast*. 2016;78:44-63.
18. Zhu Y, Kang G, Kan Q, Bruhns O, Liu Y. Thermo-mechanically coupled cyclic elasto-viscoplastic constitutive model of metals: theory and application. *Int J Plast*. 2016;79:111-152.
19. Zhang S, Xuan F. Interaction of cyclic softening and stress relaxation of 9–12% Cr steel under strain-controlled fatigue-creep condition: experimental and modeling. *Int J Plast*. 2017;98:45-64.
20. Shintaku Y, Tsutsumi S, Terada K. A CDM-like constitutive law for predicting degradation of strength and ductility of steel subjected to cyclic loading. *Int J Plast*. 2022;153:103237. doi:10.1016/j.ijplas.2022.103237
21. Zhang J, Jiang Y. Constitutive modeling of cyclic plasticity deformation of a pure polycrystalline copper. *Int J Plast*. 2008;24(10):1890-1915.
22. Zhu Y, Kang G, Yu C. A finite cyclic elasto-plastic constitutive model to improve the description of cyclic stress-strain hysteresis loops. *Int J Plast*. 2017;95:191-215.
23. Zhou J, Sun Z, Kanouté P, Retraint D. Experimental analysis and constitutive modelling of cyclic behaviour of 316L steels including hardening/softening and strain range memory effect in LCF regime. *Int J Plast*. 2018;107:54-78.
24. Wright M. The interior-point revolution in optimization: history, recent developments, and lasting consequences. *Bull Am Math Soc*. 2005;42(1):39-56.
25. Krabbenhoft K, Lyamin A, Sloan S, Wriggers P. An interior-point algorithm for elastoplasticity. *Int J Numer Meth Eng*. 2007;69(3):592-626.
26. Scheunemann L, Nigro PJS, Pimenta P. A novel algorithm for rate independent small strain crystal plasticity based on the infeasible primal-dual interior point method. *Int J Plast*. 2020;124:1-19.
27. Inagaki K, Hashimoto G, Okuda H. Interior point method based contact analysis algorithm for structural analysis of electronic device models. *Mech Eng J*. 2015;2(4):15-00146.
28. Nigro P, Simões E, Pimenta P, Schröder J. Model order reduction with Galerkin projection applied to nonlinear optimization with infeasible primal-dual interior point method. *Int J Numer Meth Eng*. 2019;120(12):1310-1348.
29. Shintaku Y, Nakamura F, Tsutsumi S, Terada K. An implicit solution for an elastic-plastic model with hardening rule depending on plastic strain range using a primal-dual interior point method. *Trans JSCES*. 2022;2022:20220001. doi:10.11421/jsces.2022.20220001
30. Lubarda V, Benson D. On the numerical algorithm for isotropic-kinematic hardening with the Armstrong-Frederick evolution of the back stress. *Comput Methods Appl Mech Eng*. 2002;191(33):3583-3596.
31. Kriegm R. A practical two surface plasticity theory. *J Appl Mech-Trans ASME*. 1975;42(3):641-646.
32. Xiao H, Bruhns O, Meyers A. Logarithmic strain, logarithmic spin and logarithmic rate. *Acta Mech*. 1997;124:89-105.

33. Yoshida F, Uemori T. A model of large-strain cyclic plasticity describing the Bauschinger effect and workhardening stagnation. *Int J Plast*. 2002;18(5):661-686.
34. Yamashita H. A globally convergent primal-dual interior point method for constrained optimization. *Optim Methods Softw*. 1998;10(2):443-469.

How to cite this article: Shintaku Y, Nakamura F, Terada K. A hybrid strategy blending primal-dual interior point and return mapping methods for a class of hypoelastic-plastic models with memory surface. *Int J Numer Methods Eng*. 2023;1-23. doi: 10.1002/nme.7195